Bull. Chem. Soc. Jpn., **77**, 1075–1100 (2004)

Accounts

Electron-Spin Dynamics and Structures in Halogen-Bridged 1-D Metal Complexes Studied by Solid NMR

Ryuichi Ikeda

Department of Chemistry, University of Tsukuba, Tsukuba 305-8571

Received November 27, 2003; E-mail: ikeda@chem.tsukuba.ac.jp

Magnetic properties characteristic in 1-D systems were investigated in halogen-bridged mixed-valence and averaged-valence metal complexes by applying magnetic resonance techniques. Neutral-solitons and polarons formed from impurity amounts of paramagnetic Pt^{3+} and Pd^{3+} sites in 1-D chains were sensitively detected by the NMR relaxation measurement. Their rapid 1-D diffusion comparable to that in *trans*-polyacetylene was revealed in $[M^{II}(en)_2]$-$[M^{VI}Br_2(en)_2](ClO_4)_4$ (M: Pt, Pd). From ^{13}C NMR spectra and ^{1}H NMR relaxation studies, $[Ni^{III}X(chxn)_2]X_2$ (X: Cl, Br) was shown to be in an averaged-valence state forming $S = 1/2$ 1-D Heisenberg antiferromagnetic chains. $[NiBr(chxn)_2]Br_2$ revealed to have the largest exchange interaction so far reported, was expected to transform into a new state at low-temperatures below 100 K. From studies on thermal motions and phase transitions associated with the 1-D chain-structure in $[Pt(en)_2][PtX_2(en)_2](ClO_4)_4$ (X: Cl, Br), the presence of the dynamic disorder of the $Pt(en)_2$ chelate-ring conformation in a highly asymmetric double-well potential undetected by the X-ray diffraction was detected by the NMR relaxation measurement.

In the history of studies on transition metal complexes, Pt complexes with one-dimensional (1-D) chain structures have attracted interests among chemists and physicists because of their characteristic structures and properties essential to this system. Magnus's green salt, $[Pt(NH_3)_4]PtCl_4$, Wolffram's red salt, $[Pt(C_2H_5NH_2)_4][PtCl_2(C_2H_5NH_2)_4]$, Krogmann's salt, $K_{1.75}Pt(CN)_4 \cdot 1.5H_2O$, etc., have received wide attention owing to their markedly colored crystalline states with abnormal dichroism. Among these, halogen-bridged 1-D Pt or Pd complexes having a di- and tetravalent mixed-valence structure expressed as $–X–M^{2+}–X–M^{4+}–X–$ have recently provided a new field, because of their unique 1-D structure and strong electron–lattice interactions.[1] Since a wide variety of halogen-bridged mixed-valence complexes generally expressed as $[M^{II}L_4]$-$[M^{IV}X_2L_4]A_4$ (M: Pt, Pd; L: ligand; X: Cl, Br, I; A: counter anion) have been synthesized with various combinations of M, L, X, and A;[2] hence, we can prepare 1-D systems with various degrees of electron–lattice interactions by controlling interactions between metals or chains with suitable choices of these building blocks. In this system, the 1-D structure is markedly deformed and the bridged halogen atoms are displaced from the mid-point between M^{2+} and M^{4+} sites.[3] This deformed structure is called a *charge-density-wave* (CDW) state. As an example, the crystal structure of $[Pt(en)_2][PtBr_2(en)_2]$-$(ClO_4)_4$ (en: ethylenediamine)[4] is shown in Fig. 1.

Another remarkable crystal structure in this system is the mutually disordered arrangements of M^{2+} and M^{4+} sites between neighboring 1-D chains as shown in Fig. 1. This structure implies that quite weak or homogeneous interactions work between chains, enabling characteristic optical properties due to the charge transfer between metal sites with different valences as well as electron spin migrations in forms of *solitons* and *polarons* obtainable in highly isolated 1-D systems like *trans*-polyacetylene.[5] Since motions of these quasi-particles can produce

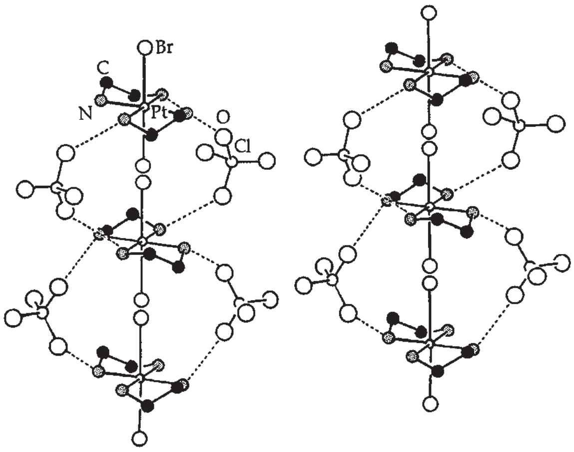

Fig. 1. The 1-D structure in a CDW complex, $[Pt(en)_2]$-$[PtBr_2(en)_2](ClO_4)_4$ determined by the X-ray diffraction. Two Br atoms located close to each other along the chain show that the mutual arrangement of Pd^{2+}–Pd^{4+} positions between the neighboring chains is disordered.

DOI 10.1246/bcsj.77.1075

fluctuations in magnetic interactions in crystals, the detection of these particles even in a low concentration can effectively be carried out by magnetic resonance techniques.

The CDW state in halogen-bridged complexes can be stably formed by a simple model in which the electron–phonon interactions (S) in the 1-D chain are greater than the on-site Coulombic interaction (U) between d-electrons in a metal atom.[6] Oppositely, if we can prepare any 1-D system with $U > S$, an averaged-valence complex with a *spin-density-wave* (SDW) state can be realized. Recent studies on 1-D halogen-bridged complexes, $[NiX(chxn)_2]X_2$ (X: Cl, Br; chxn: 1*R*,2*R*-cyclohexanediamine) revealed that all Ni atoms on the 1-D chain are equivalent,[7] suggesting the formation of 1-D chains of paramagnetic Ni^{3+}. These complexes are expected to be an $S = 1/2$ 1-D *Heisenberg antiferromagnetic system*, which has attracted attention because of remarkable quantum effects requiring the disappearance of the long-range spin order even in the limit of 0 K. The magnetic susceptibility measurement has suggested that $[NiBr(chxn)_2]Br_2$ is a 1-D system with unprecedentedly strong antiferromagnetic interactions between neighboring Ni atoms.[8] Magnetic resonance methods can also provide detailed pictures on local spin structures and dynamics in this antiferromagnetically coupled 1-D spin system.

In the present paper, 1-D spin structures and dynamics characteristically observed in solid halogen-bridged mixed and averaged-valence metal complexes studied by magnetic resonance techniques are discussed.

1. Solitons and Polarons in Halogen-Bridged CDW Complexes

A characteristic electronic structure in halogen-bridged CDW complexes is the degenerated electronic ground state originating from the mixed-valence structure, which is quite analogous to that in *trans*-polyacetylene.[9] Two degenerated electronic ground states are schematically shown in Fig. 2a. As elementary excitations from these ground states, models of solitons and polarons formed by strongly coupled electron–lattice interactions are shown in Figs. 2b to 2d. In the present case, domain walls formed at the boundary of degenerated two electronic structures with different phases, i.e., –2–4–2–4– and –4–2–4–2– can migrate along the chain over long ranges by forming "*neutral solitons*" expressed as –2–4–***3***–2–4– including a paramagnetic M^{3+} site as shown in Fig. 2b. For the neutral soliton, a phase mismatch occurs at the boundary, and, at the same time, no extra charge appears on the chain even when a trivalent site is inserted. When divalent or tetravalent metal sites are inserted at the boundary, *charged solitons* with a positive or a negative charge are formed. As an example, a model of the positive-charge soliton is shown in Fig. 2c. In this case, a phase mismatch with no paramagnetic spins takes place, but an extra charge compensating the soliton charge has to be present nearby for keeping the charge neutrality. It is remarkable that neutral solitons migrate along the chain by accompanying spins but no charges. This process is schematically shown in Fig. 3, where an electron in a trivalent site jumps alternately to the opposite direction[9] while reversing the spin direction resulting in no charge motion, but only the spin migration. Oppositely, charged solitons carry no spins but carry positive or negative charges.

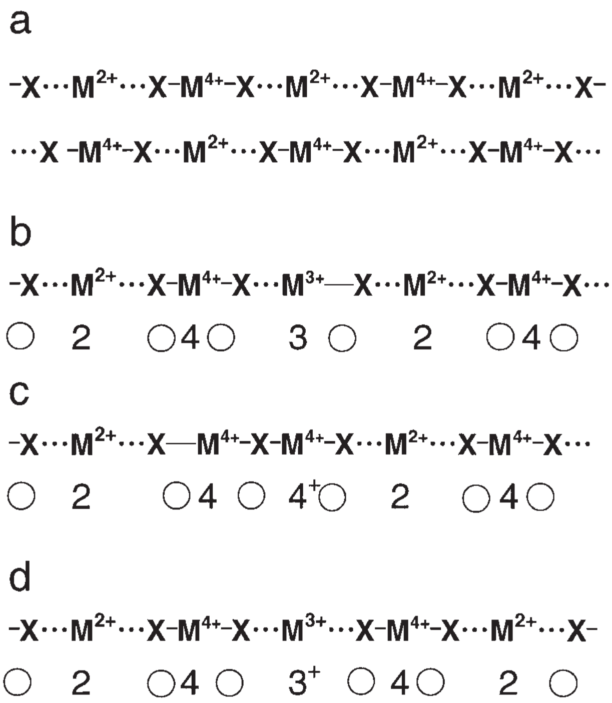

Fig. 2. Metal valence-state models in halogen-bridged 1-D CDW metal complexes. Numbers show the valence on metals. Rough positions of halogen atoms are shown by circles. a. Degenerated electronic ground states. b. A schematic model of a neutral spin-soliton formed in a 1-D chain. c. A schematic model of a positively charged soliton. d. A schematic model of a polaron with a positive charge.

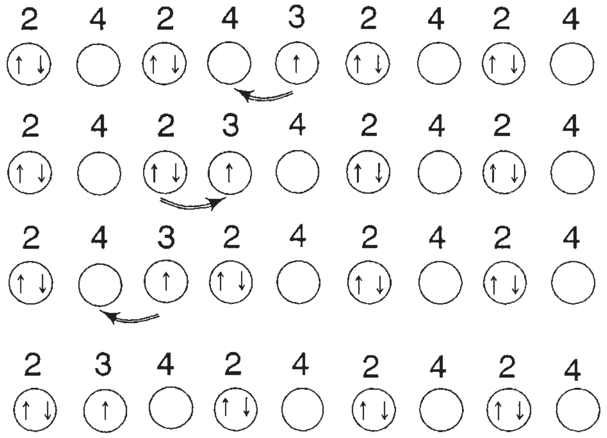

Fig. 3. A neutral soliton model of the spin migration along the 1-D chain. Numbers present valences on metal atoms and up and down arrows are spins in the d_{z^2} orbital. Curved arrows show the direction of the spin migration. The change from the top to the bottom in the figure shows the soliton motion from right to left.

As for the *polaron*, no mismatch in the 1-D structure as in solitons is required as shown in Fig. 2d, but paramagnetic M^{3+} sites with an extra charge and the lattice deformation migrate together as given by –2–4–$\boldsymbol{3}^{+}$–4–2– or –4–2–$\boldsymbol{3}^{-}$–2–4–. Since charges on polarons cannot be compensated on the chain, the existence of extra charges in the neighborhood is indispensable. Neutral solitons and polarons are characterized by the formation and 1-D diffusion of paramagnetic M^{3+} sites. These dynamic phenomena concerned with paramagnetic spins are detectable with high sensitivities by magnetic resonance methods; especially, neutral solitons in which only spins migrate with no charge motion are suitable to be observed by NMR and ESR techniques.

2. Solitons in 1-D CDW Complexes $[M(en)_2][MBr_2(en)_2](ClO_4)_4$ (M: Pt, Pd)

A unique property in 1-D diamagnetic CDW complexes $[M(en)_2][MX_2(en)_2](ClO_4)_4$ (M: Pt, Pd; X: Cl, Br) is that ESR signals can be observed. It have been reported[10] that $[Pt(en)_2][PtX_2(en)_2](ClO_4)_4$ (en: ethylenediamine; X: Cl, Br) gives ESR signals assignable to paramagnetic Pt^{3+} without any doping. A temperature dependence of ESR spectra of polycrystalline $[Pd(en)_2][PdBr_2(en)_2](ClO_4)_4$ (**1**) measured by our group[11] is shown in Fig. 4. The presence of paramagnetic Pd^{3+} sites was shown by referring to the spectrum analysis of Pt complexes.[10] The observed linewidth, showing a gradual reduction upon heating, was attributed to the motional narrowing of thermally excited electron spins in the crystal. The spin concentration determined in **1** was almost temperature independent and was estimated to be ca. 10^{-4} per Pd site. Temperature dependent ESR spectra in a polycrystalline sample of $[Pt(en)_2][PtBr_2(en)_2](ClO_4)_4$ (**2**) were also measured and quite analogous results to that in **1** were obtained.[11] The evaluated spin density was ca. 10^{-4}, in agreement of the reported value of 2.8×10^{-4} measured on single crystals.[10] These results indicate that a small amount of M^{3+} sites are formed in the process of the polymerization of 1-D chains in **1** and **2**.

The NMR relaxation measurement is a sensitive probe for obtaining the information from a small amount of paramagnetic spins, because even a trace of electron spins can make a strong relaxation mechanism owing to the magnetic moment of an electron being ca. 10^3 times larger than those in nuclei. The ^{1}H NMR spin-lattice relaxation time (T_1) measurement performed below room temperature in **1** and **2**[11] showed the presence of two kinds of protons, with fast and slow relaxations, and the relative magnitude of these two kinds of ^{1}H magnetizations showed temperature-dependent behavior, namely, the magnetization of the fast component rapidly decreased upon heating.

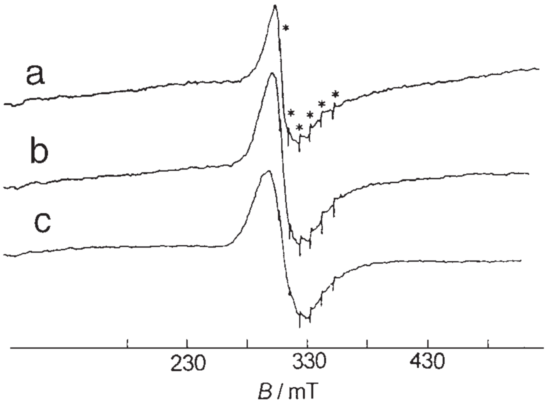

Fig. 4. A temperature dependence of derivative curves of ESR spectra observed in a powder sample of a CDW complex $[Pd(en)_2][PdBr_2(en)_2](ClO_4)_4$ at 293 K (a), 213 K (b), and 133 K (c). Lines with asterisks are maker signals from doped Mn^{2+} in MgO (Ref. 11).

The rapidly relaxing component did not give a single T_1 but gave distributed T_1 values. This component was assigned to protons located in the neighborhood of trapped or fixed paramagnetic M^{3+} sites on chains and/or at chain ends in crystals shown in Fig. 5(a) as a schematical model. This is because protons located near fixed M^{3+} sites, i.e., protons in spheres in the figure (shown by circles as a two-dimensional model) feel the fluctuation of the strong magnetic field made by fixed electron spins, and their T_1 values depend on the proton–electron distance.

On the other hand, for protons far enough away from paramagnetic Pt^{3+} sites, the spin-diffusion mechanism, which enables the nuclear-magnetization propagation via mutual flips of spins in neighboring protons with no mass migration, becomes dominant over electron–proton magnetic dipolar interactions.

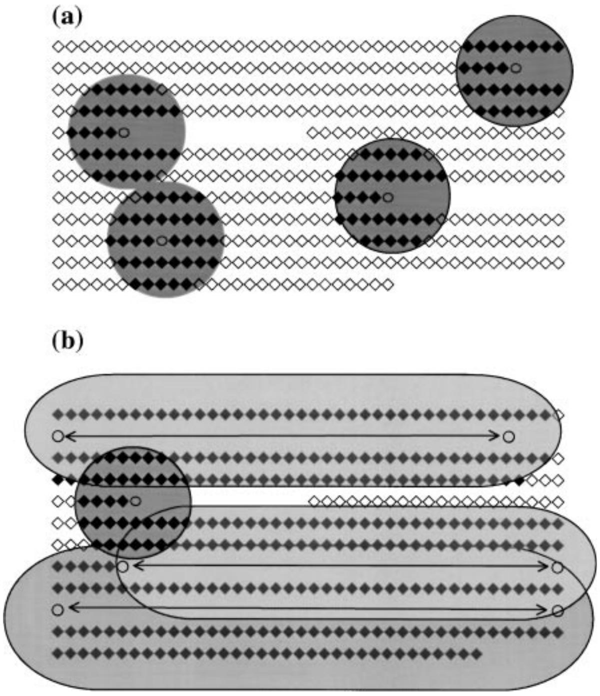

Fig. 5. Schematic 2-D models of electron–proton magnetic dipolar interactions in a 1-D chain system on which (a) paramagnetic M^{3+} sites are fixed at low temperatures, while (b) they diffuse along chains by obtaining thermal activation energies at high temperatures. Chains of squares (◇◇◇), dots ○, and the darkly shaded part in circles present the $–X–M^{2+}–X–M^{4+}–X–$ chains, paramagnetic metal (M^{3+}) sites and protons receiving a strong fluctuation of the magnetic field made by electron spins, respectively. Protons in the dark shade in (a) give distributed short T_1 values, while protons in the outside circles exhibit a constant long T_1 controlled by the spin-diffusion mechanism. In (b), protons in the light shade feel an averaged fluctuation of magnetic field made by rapidly diffusing electron spins.

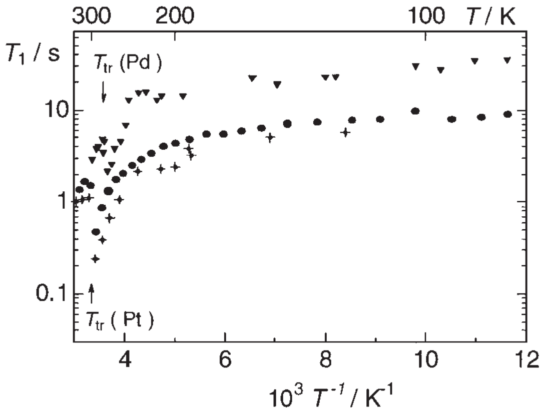

Fig. 6. ^{1}H T_1 of the slowly relaxing component observed in $[Pd(en)_2][PdBr_2(en)_2](ClO_4)_4$ (**1**) at 40.4 MHz (▼) and $[Pt(en)_2][PtBr_2(en)_2](ClO_4)_4$ (**2**) at 20.96 (+) and 40.14 MHz (●). T_{tr} is the phase-transition temperature.

Protons located in this region give a constant T_1 corresponding to the observed long T_1 component. Determined T_1 values of the slow component in **1** and **2** are shown in Fig. 6. A gradual T_1 decrease upon heating from ca. 85 up to 200 K was observed for both **1** and **2**, then a sharp decrease to phase transition temperatures (T_{tr}) was obtained.

From the temperature dependent ^{1}H relaxation together with the ESR data revealing that paramagnetic Pt^{3+} and Pd^{3+} densities in crystals are almost temperature-independent,[10,11] the following model of the spin dynamics can be derived: Paramagnetic sites fixed in 1-D chains at low temperatures shown in Fig. 5(a) begin to move apart from the trapped sites upon heating thanks to obtaining the thermal excitation energy. This means that fixed paramagnetic spins decrease in number, while the moving spin number increases with temperature, consistent with the observed results. Upon heating, the protons along the chain feel an averaged magnetic field made by rapidly diffusing electrons. From these considerations, the increase in the proton number having the long T_1 and the gradual decrease of the T_1 value on heating could be explained as schematically shown in Fig. 5(b).

The present model of the electron-spin migration can be supported by the temperature dependence studies of the ESR linewidth shown in Fig. 4 for the present **1** and in Ref. 10 for **2**; both showed a gradual narrowing upon heating attributable to the motional effect.

The rapid decrease of the fast T_1 component observed in both complexes above ca. 200 K shown in Fig. 6 is attributable to the effect from the phase transition, which shortens ^{1}H T_1 due to lattice motions, as discussed in Sec. 7.

For the quantitative discussion of the observed T_1, the dimensionality of the electron-spin motion has to be investigated in connection with the Larmor-frequency dependence of T_1. The nuclear relaxation by rapidly diffusing electrons in low-dimensional systems has theoretically been studied.[12,13] It has been reported that the nuclear relaxation rate due to randomly jumping electron spins, under the condition that the diffusion rate D^* of spins fulfills $D^* \gg \omega_e, \omega_N$, where ω_e and ω_N are electron and nuclear Larmor frequencies, respectively, is given by[13]

$$T_1{}^{-1} = kT\chi_s\left[\frac{3}{5}d^2 f(\omega_N) + \left(a^2 + \frac{7}{5}d^2\right)f(\omega_e)\right], \tag{1}$$

where $f(\omega)$ denotes the spectrum density, and d, a, and χ_s are anisotropic (dipolar) and isotropic (scalar) parts of the hyperfine coupling between protons and electrons, and the normalized electron susceptibility per metal site, respectively. When electrons diffuse along 1-D chains, The spectrum density $f_{1D}(\omega)$ is expressed as[12]

$$f_{1D}(\omega) = \frac{1}{\sqrt{2D^*\omega}} - \frac{2\gamma\lambda}{2D^*}, \tag{2}$$

where λ is called the delocalization length and γ is given by 0.33 when $\lambda > 5$. D^* is defined using the 1-D diffusion constant D and the inter-site distance b in the chain as $D^* = D/b^2$. In case electrons diffuse in 2-D and 3-D lattices, the spectrum densities $f_{2D}(\omega)$ and $f_{3D}(\omega)$, respectively, depend on D^* and ω differently from $f_{1D}(\omega)$ and are written by

$$f_{2D}(\omega) \propto \frac{1}{2\pi\sqrt{D_1{}^*D_2{}^*}}\ln\frac{4\pi^2 D_2{}^*}{\omega}, \tag{3}$$

where $D_1{}^*, D_2{}^* > \omega$,
and

$$f_{3D}(\omega) \propto \frac{1}{2\pi\sqrt{D_1{}^*D_2{}^*}}\ln\frac{4\pi^2 D_2{}^*}{D_3{}^*}, \tag{4}$$

where $D_1{}^*, D_2{}^*, D_3{}^* > \omega$. It is noted that the spectrum density in the 3-D diffusion is independent of ω.

In the present 1-D diffusion model, the coupling between proton and electron spins is approximately assumed to be dipolar, then Eq. 1 is rewritten as

$$T_1^{-1} \cong kT\chi_s\left[\frac{3}{5}d^2 f_{1D}(\omega_N) + \frac{7}{5}d^2 f_{1D}(\omega_e)\right]. \tag{5}$$

If one combines Eqs. 2 and 5, the ^{1}H T_1 contributed from the 1-D diffusing electron spins can be finally written by

$$T_1{}^{-1} = kT\chi_s\frac{d^2}{5}\left[\left(3 + 7\sqrt{\frac{\gamma_H}{\gamma_e}}\right)\frac{1}{\sqrt{2D^*\omega_H}} - \frac{3.3\lambda}{D^*}\right]. \tag{6}$$

If one applies Eq. 6, D^* and λ can be derived from experimental data. Larmor frequency dependences of T_1 observed in **1** and **2** shown in Fig. 7 can be well interpreted by Eq. 6, supporting the 1-D diffusion of electron spins. From the slope of the plots, the diffusion rate D^* can be estimated by using the dipolar coupling constant d calculated from the crystal data, and χ_s can be estimated by assuming that the concentration of the diffusing electron-spins is proportional to the magnetization of the slow component.

Temperature dependences of D^* determined for **1** and **2** are shown in Fig. 8. D^* in **2** became 4 to 10×10^{12} rad s^{-1}, while **1** gave two orders of magnitude higher values than **2** gave. The unusual D^* decrease upon heating observed above ca. 180 K for both complexes seems to be due to lattice motions hindering the electron spin migration. Since it has been reported that a change in structure of the zig-zag 1-D chain takes place at T_{tr},[14,15] marked thermal vibrations of skeletons of 1-D chains are expected near T_{tr}.

From Fig. 8, the activation energy (E_a) for the electron-spin

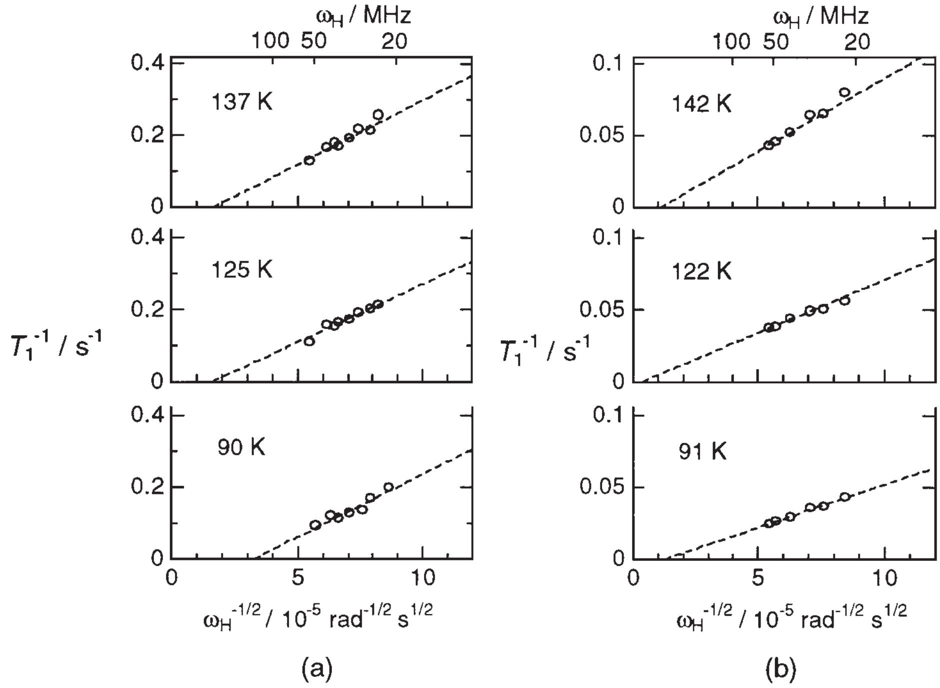

Fig. 7. Larmor frequency (ω_H) dependences of ^{1}H T_1 of the slowly relaxing component observed in (a) [Pt(en)$_2$][PtBr$_2$(en)$_2$](ClO$_4$)$_4$ (**2**) and (b) [Pd(en)$_2$][PdBr$_2$(en)$_2$](ClO$_4$)$_4$ (**1**). Broken lines are fitted theoretical values using Eq. 6 in text.

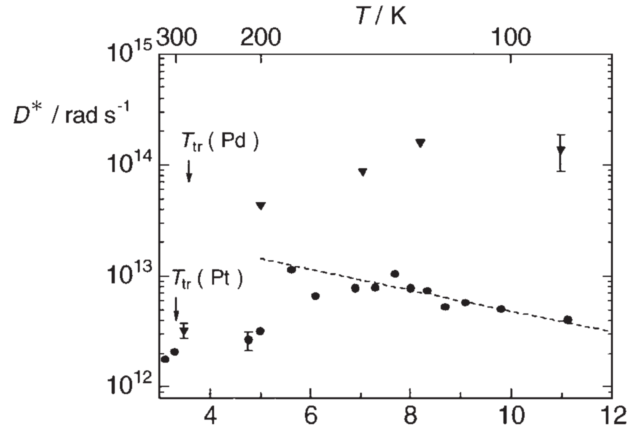

Fig. 8. Temperature dependences of the 1-D diffusion rate D^* of electron spins in [Pt(en)$_2$][PtBr$_2$(en)$_2$](ClO$_4$)$_4$ (**2**) (●) and [Pd(en)$_2$][PdBr$_2$(en)$_2$](ClO$_4$)$_4$ (**1**) (▼). The slope of the broken line gives the activation energy of 17 meV. T_{tr} is the phase-transition temperature.

diffusion in **2** was estimated to be 17 ± 2 meV by assuming the Arrhenius relation for the temperature dependence of D^*. This estimation was difficult for **1**, but it seems to be smaller than that in **2**. It is noted that this E_a obtained in **2** is much lower than $E_a = 840$ meV determined from electrical conductivity data.[16] If the unpaired spin is assumed to be the charge-carrier contributing to the conductivity σ, the 1-D conductivity σ_{NMR} derived from NMR is expressed with the obtained D^* using the Nernst–Einstein relation given by

$$\sigma_{NMR} = \frac{ne^2b^2D^*}{kT}. \tag{7}$$

Here, n and e are the charge-carrier concentration and the electronic charge, respectively. $\sigma_{NMR} = 10^{-1}$ S m^{-1} was obtained at 303 K by substituting determined D^* values and reported values[10,15] of n and b into Eq. 7, giving a 10^7 times higher conductivity than 10^{-9} S m^{-1} reported[16] for **2**. From this disagreement between the NMR and the electrical conductivity results, the carriers of spin and charge are considered to be different in the present system. This indicates that the diffusing spin carriers detected from ^{1}H T_1 can mostly be attributed to neutral solitons.

Parameters for electron spins obtained in **1** and **2** can be compared with analogous results reported for *trans*-polyacetylene,[17] in which the formation of neutral-solitons was shown in 1-D CH chains. Table 1 shows dynamic parameters in these systems obtained in 100–150 K together with data of an analogous CDW complex [Pd(chxn)$_2$][PdBr$_2$(chxn)$_2$]Br$_4$ (**3**)[18] which will be discussed in Sec. 4. It is noteworthy that nearly the same soliton concentration and diffusion rate were obtained in the present complexes and in *trans*-polyacetylene having quite different electronic structures with each other. An unpaired electron spin forming a soliton is expected to delocalize over several metal sites. This soliton-delocalization width (λ) was roughly estimated from frequency dependent T_1 data shown in Fig. 7 using Eq. 6. Estimated λ values are shown in Table 1. These values are consistent with the theoretical estimation of $\lambda \cong 12$ calculated for halogen-bridged mixed-valence complexes.[19–21]

3. Soliton Formation in Mixed-Metal CDW Complexes [Pd^{II}(en)$_2$][Pt^{IV}X$_2$(en)$_2$](ClO$_4$)$_4$ (X: Cl, Br)

In the foregoing section, it was shown that a small amount of paramagnetic M^{3+} sites formed in 1-D chains of [M(en)$_2$][MBr$_2$(en)$_2$](ClO$_4$)$_4$ (M: Pd, Pt) can be detected by NMR and

Table 1. Spin-Soliton Concentrations (n) at Room Temperature, Soliton Diffusion Rates (D^*) and Activation Energies (E_a) in 90–150 K, the Delocalization Length (λ) of a Soliton and Electrical Conductivities (σ) at Room Temperature Evaluated in $[Pd(en)_2][PdBr_2(en)_2](ClO_4)_4$ (**1**), $[Pt(en)_2][PtBr_2(en)_2](ClO_4)_4$ (**2**) Together with Those in $[Pd(chxn)_2][PdBr_2(chxn)_2]Br_4$ (**3**) Discussed in Sec. 4 and *trans*-Polyacetylene for Comparison

Compound	n	D^*/rad s^{-1}	E_a/meV	λ/site	σ/S m^{-1}
$[Pd(en)_2][PdBr_2(en)_2](ClO_4)_4$	10^{-4}	$(9\text{–}20) \times 10^{13}$	—	20–120	$10^{-6\,\mathrm{b)}}$
$[Pt(en)_2][PtBr_2(en)_2](ClO_4)_4$	$10^{-4\,\mathrm{a)}}$	$(4\text{–}10) \times 10^{12}$	17	30–50	$10^{-9\,\mathrm{b)}}$
$[Pd(chxn)_2][PdBr_2(chxn)_2]Br_4$	$10^{-3\,\mathrm{c)}}$	$10^{11}\text{–}10^{12\,\mathrm{c)}}$ $(10^{13})^{**}$	$10^{\mathrm{c)}}$ $(140)^{**}$	$20^{\mathrm{c)}}$	$10^{-1\,\mathrm{d)}}$
trans-Polyacetylene	$10^{-3}\text{–}10^{-4\,\mathrm{e)}}$	$2\text{–}4 \times 10^{13\,\mathrm{e)}}$	—	$17^{\mathrm{e)}}$	$10^{-3\,\mathrm{f)}}$

Data in parentheses are evaluated at temperature higher than 200 K and assignable to polarons. a) Ref. 10. b) Ref. 16. c) Ref. 8. d) Ref. 30. e) Ref. 29. f) H. Shirakawa, T. Ito, and S. Ikeda, *Polym. J.*, **4, 460 (1973).

ESR measurements, and that their dynamic behavior is well explained by the 1-D electron-spin diffusion model proposed by Devreux et al.[12,13] The main origin of observed diffusing spins was expected to be domain-wall type neutral spin-solitons. As another origin of diffusing paramagnetic sites, the possibility of the polaron formation could not be completely excluded.

As a suitable system for distinguishing these two types of electron-spin diffusion mechanisms, a new type of CDW complexes consisting of hetero-metals, expressed as $[Pd^{II}(en)_2][Pt^{IV}X_2(en)_2](ClO_4)_4$ (X: Cl, Br) were prepared.[22] The crystal structure[23] of hetero-metal complexes was shown to be isomorphous with that in the corresponding homo-metal complexes $[M^{II}(en)_2][M^{IV}X_2(en)_2](ClO_4)_4$ (M: Pt, Pd; X: Cl, Br) with the same structure. A characteristic feature in hetero-metal complexes is that the electronic ground state of the metal–halogen chain, which is degenerated in homo-metal complexes, is non-degenerate because –2–4– and –4–2– structures are no longer the same when their valencies are interchanged. As shown in Fig. 3, when a soliton moves along a 1-D chain, a valence exchange between divalent and tetravalent metal sites also occures. This suggests that the structure with the non-degenerated electronic ground state is unfavorable for the soliton migration. In this section, the foregoing explanation of the diffusing electron spins as neutral solitons in the homo-metal complexes with the degenerated ground state is discussed by using the data from temperature dependence measurements of ESR spectra and ^{1}H NMR T_1 in the hetero-metal complexes.

ESR spectra in polycrystalline samples of hetero-metal complexes, $[Pd^{II}(en)_2][Pt^{IV}X_2(en)_2](ClO_4)_4$ (X: Cl (**4**), Br (**5**)) were remarkably weakened[24] compared with those in corresponding homo-metal complexes, but showed roughly the same lineshapes and widths as in the homo system.[10] A comparison of spectra observed in a homo- and a hetero-metal complex with almost the same sample quantity and under analogous experimental conditions is shown in Fig. 9. Both **4** and **5** gave spin concentrations of ca. 10^{-5} in the metal molar ratio which is roughly one-tenth of those in the corresponding homo-complexes. From the low-concentrations of paramagnetic M^{3+} sites observed in the complexes with the non-degenerated ground state, the foregoing interpretation that most of the paramagnetic spins in the homo-metal complexes form neutral solitons is acceptable. The present explanation is consistent with an optical study[25] that reveals that the photo-generation of solitons is suppressed in the hetero-metal complexes.

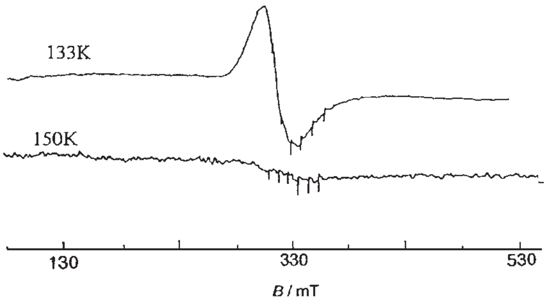

Fig. 9. A comparison of ESR spectra observed in a homo- and a hetero-metal complex under analogous conditions: $[Pd(en)_2][PdBr_2(en)_2](ClO_4)_4$ (**1**) (upper) and $[Pd(en)_2]$-$[PtBr_2(en)_2](ClO_4)_4$ (**5**) (lower). Sharp peaks are maker signals from Mn^{2+}.

The ^{1}H NMR spin-lattice relaxation measurement in hetero-metal complexes **4** and **5** afforded the temperature-dependent T_1 values shown in Figs. 10 and 11, respectively, where the data obtained in homo-complexes $[M(en)_2][MX_2(en)_2](ClO_4)_4$ (M: Pt, Pd; X: Cl, Br) are shown for comparison.

The characteristic T_1 behavior observed for the hetero-metal complexes in the low-temperature range is that observed T_1 values were much longer than those in homo-metal –Pd–X–Pd– and Pt–X–Pt– complexes, and did not show intermediate values. This result also can be explained by considering that the concentration of paramagnetic M^{3+} sites in hetero-metal complexes is much lower than that in the homo-complexes. This explanation is consistent with the suppression of the neutral soliton in systems having the non-degenerated electronic ground state.

Another feature of T_1 is its rapid decrease on heating above ca. 200 K as observed in **4** and **5**. This is explainable by lattice motions associated with phase transitions occurring at room temperature.[15] Detailed discussion is given in Sec. 7.

As possible origins of the small amount of paramagnetic sites observed in the hetero-metal complexes, the formation of polarons and fixed paramagnetic impurities at ends of chains can be proposed. Here, the model of polarons seems to be more acceptable, if one considers the ^{1}H magnetization recovery curves observed in **4** and **5** and shown in Fig. 12. These curves show that an almost single relaxation process contributes to both **4** and **5**, indicating that most protons in crystals feel the same order of strength in magnetic field fluctuations made by

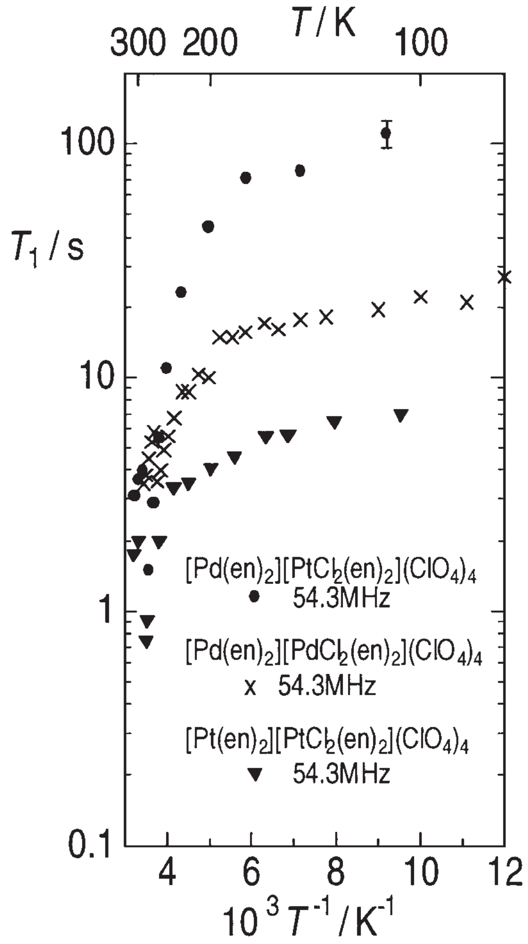

Fig. 10. Temperature dependences of spin-lattice relaxation time T_1 in a hetero-metal complex [Pd(en)$_2$][PtCl$_2$(en)$_2$]-(ClO$_4$)$_4$ (**4**) and homo-metal complexes [M(en)$_2$]-[MCl$_2$(en)$_2$](ClO$_4$)$_4$ (M: Pt, Pd) for comparison.

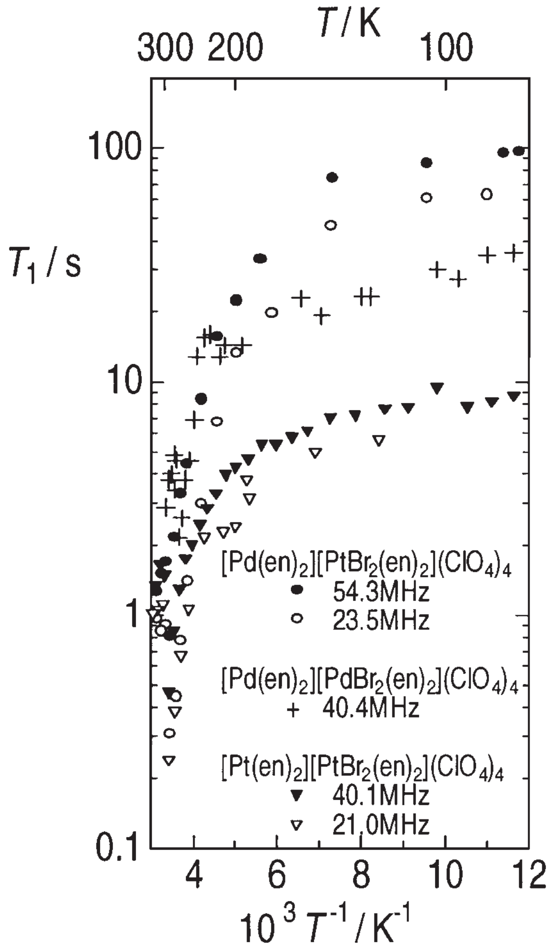

Fig. 11. Temperature dependences of spin-lattice relaxation time T_1 in a hetero-metal complex [Pd(en)$_2$][PtBr$_2$(en)$_2$]-(ClO$_4$)$_4$ (**5**) and homo-metal complexes [M(en)$_2$]-[MBr$_2$(en)$_2$](ClO$_4$)$_4$ (M: Pt, Pd) for comparison.

electron spins. From the discussion in Sec. 2, this relaxation behavior originating from the impurity order of paramagnetic spins can be explained by the rapid diffusion of the paramagnetic sites which make a fluctuation of magnetic field averaged over all the sample. This kind of rapid motion seems difficult for trapped paramagnetic impurities at ends of chains, but is explainable by the polaron model.

4. Dynamics of Paramagnetic Spins in [Pd(chxn)$_2$][PdBr$_2$(chxn)$_2$]Br$_4$

4.1 A CDW Complex with a Small Distortion. A wide variety of halogen-bridged CDW Pt and Pd complexes have been prepared by the combination of central metals, bridged halogens, ligands, and counter anions. In the CDW state, where bridging halogen atoms are located at an off-centered position between neighboring metal sites, displacements of halogen positions from the midpoint of two metal sites take different values dependent upon constituent metals, halogens, ligands, and counter ions. Among so far reported halogen-bridged CDW complexes, [Pd(chxn)$_2$][PdBr$_2$(chxn)$_2$]Br$_4$ (**3**) (chxn: 1*R*,2*R*-cyclohexanediamine), has been shown to have the smallest CDW distortion[26] indicating that **3** has an electronic structure close to the averaged-valence structure consisting of the –3–3–3–3– type 1-D chain. The crystal structure of **3** determined by the X-ray diffraction is shown in Fig. 13.[27]

It has been reported that **3** shows 0.75 eV[8] for the charge-transfer excitation energy from the occupied Pd^{2+} d_{z^2} orbital to the neighboring vacant Pd^{4+} d_{z^2} orbital. This value is much lower than those in the other CDW complexes such as **1** and **2**, which gave 1.22 and 1.95 eV, respectively.[28] These facts suggest that paramagnetic M^{3+} sites in **3** can be formed much more easily compared with those in **1** and **2**. In fact, the ESR study on **3** revealed[8] that the concentration of paramagnetic sites is ca. 4×10^{-3} per Pd site. This value is ten times more than the concentrations determined in **1** and **2**.[11] The observed spin susceptibility was shown to follow the Curie law at low temperatures below 100 K, indicating a temperature-independent concentration of paramagnetic sites in 1-D chains, as observed in **1** and **2**. At high temperatures, however, the spin concentration deviated from the susceptibility expected from the Curie law and showed a temperature dependent increase.[8] This suggests that paramagnetic spins are formed by the themal excitation.

On the other hand, 1-D chains in **3** form 2-D hydrogen bond networks through counter Br$^-$ ions as shown in Fig. 13, in contrast to the almost isolated 1-D chain structure in ethylenediamine complexes like **1** and **2**. Influence of the 2-D interactions

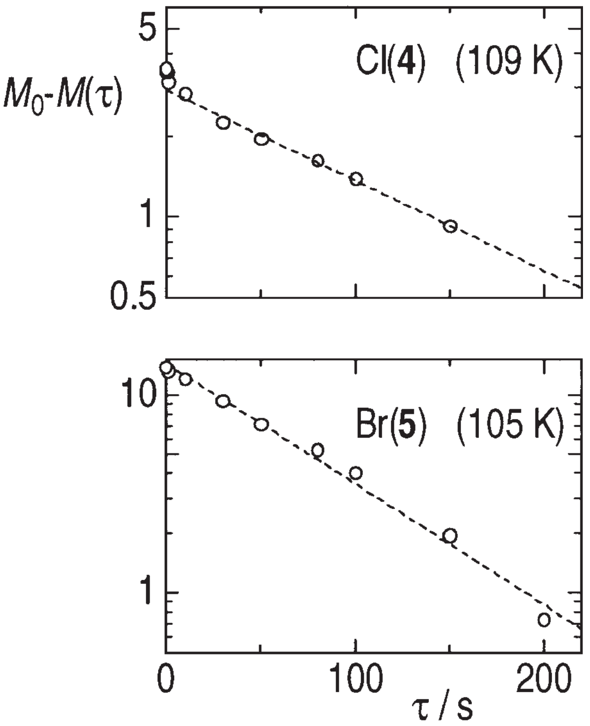

Fig. 12. ^{1}H magnetization (M) recovery curves observed after π–τ–$\pi/2$ pulses in $[Pd(en)_2][PtX_2(en)_2](ClO_4)_4$ (X: Cl (**4**), Br (**5**)) at a Larmor frequency of 54.3 MHz.

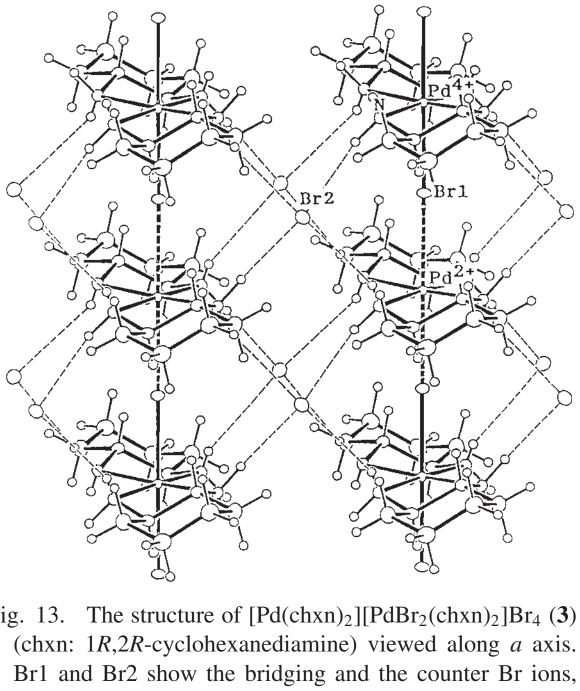

Fig. 13. The structure of $[Pd(chxn)_2][PdBr_2(chxn)_2]Br_4$ (**3**) (chxn: 1*R*,2*R*-cyclohexanediamine) viewed along *a* axis. Br1 and Br2 show the bridging and the counter Br ions, respectively. Dashed lines exhibit hydrogen bonds (Ref. 8).

in **3** to the soliton dynamics is also an interesting subject.

ESR studies[8] reported the presence of two types of paramagnetic Pd^{3+} sites in **3**, namely, Curie spins (C-spins) and thermally activated spins (TA-spins). Since a marked spectrum narrowing was observed in ESR spectra above ca. 100 K,[8] TA-spins can be assigned to Pd^{3+} sites diffusing along the chain, as shown in Fig. 5b. At the same time, the spin susceptibility which follows the Curie law below 100 K, showed a marked increase above that temperature. This implies an increase of TA-spins upon heating. This can be explained by considering that the TA-spins paired and trapped in the 1-D chain at low temperatures can separately diffuse by obtaining the activation energy upon heating.

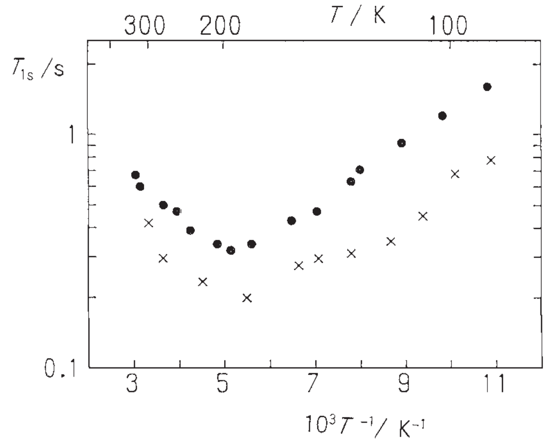

Fig. 14. Temperature dependences of T_{1S} (the rapidly relaxing component) of ^{1}H NMR observed in $[Pd(chxn)_2]$-$[PdBr_2(chxn)_2]Br_4$ (**3**) crystals at Larmor frequencies of 60.0 (●) and 30.0 (×) MHz.

C-spins with the magnetic susceptibility following the Curie law below 100 K seem to be isolated spins formed at ends of chains and fixed at lattice imperfections, and can be changed into TA-spins upon heating. TA- and C-spins in **3** are expected to correspond to two kinds of ^{1}H NMR relaxation processes, as observed in complexes **1** and **2** described in Sec. 2. In **3**, two kinds of relaxation components were roughly obtained in the temperature range studied, where the rapidly relaxing component, which showed definite T_1 values, was major and occupied 80 to 90% in the total ^{1}H magnetization.

Figure 14 shows the observed temperature dependence of the short T_1 component (T_{1S}), which was assigned to the relaxation due to TA-spins. Such relaxation data can be explained by the foregoing 1-D electron diffusion model with the spin delocalization applied to complexes **1** and **2** in Sec. 2, where T_1 was expressed as Eq. 6.[12,13] Here, it is also assumed that the coupling between protons and electrons is purely dipolar.

Figure 15 shows $T_{1S}{}^{-1}$ plotted against $\omega_H{}^{-1/2}$ observed at 303, 198, and 125 K. These plots were well interpreted by Eq. 6, supporting the existence of 1-D diffusive electron spins in **3**. According to Eq. 6, the slope of plots and the intercept on the $\omega_H{}^{-1/2}$ axis afford the diffusion rate D^* and the delocalization parameter λ, respectively, by using the dipolar parameter $d_{TA}{}^2 = 4.73 \times 10^{14}$ rad^4 s^{-2} derived from the crystal structure,[15] and χ_S from TA-spins obtained from the molar susceptibility χ_m of the TA-spins per Pd-site, since the averaged TA-spin susceptibility per Pd-site can be assumed to be χ_S. Then,

$$kT\chi_S = \frac{kT\chi_m}{N_a g^2 \mu_B^2}, \tag{8}$$

where g is 2.077 obtained as the powder average of the reported $g_\perp$ and $g_\parallel$,[8] and χ_m was given by

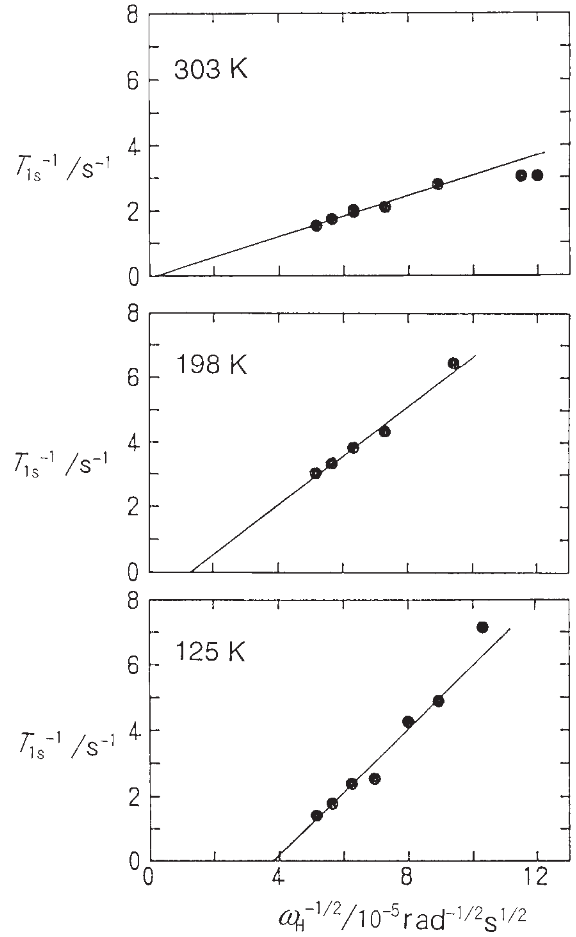

Fig. 15. Larmor frequency dependences of the short component (T_{1S}) observed in [Pd(chxn)$_2$][PdBr$_2$(chxn)$_2$]Br$_4$ (**3**) crystals. The solid lines are fitted using Eq. 6 (see text).

$$\chi_m = \frac{A}{T}\exp\left(-\frac{\Delta}{kT}\right), \tag{9}$$

where $A = 3.75 \times 10^{-3}$ emu K mol^{-1} and $\Delta/k = 370$ K. From above calculations, D^* and the delocalization length λ were evaluated. D^* and λ values obtained were, however, unacceptable because negative values of the spectrum density $f_{1D}(\omega_e)$ were derived from Eq. 2. Since this implies that $f_{1D}(\omega_e)$ is no longer described by Eq. 2 at these temperatures, the following approximated T_{1TA} was assumed instead of Eq. 6:

$$T_{1TA}^{-1} = kT\chi_S\frac{3}{5}d_{TA}^2\left[\frac{1}{\sqrt{2D^*\omega_H}} - \frac{0.66\lambda}{2D^*}\right]. \tag{10}$$

This relation can be derived by assuming that $f_{1D}(\omega_e) = 0$ in Eq. 1. Then, D^* and λ were obtained from data in Fig. 15 using Eq. 10. Obtained results are shown in Table 2, where the D^* increase on heating suggests that the diffusion of paramagnetic spins along 1-D chains is caused by the thermal activation process. These spins were roughly evaluated to be delocalized over ca. 10–20 Pd-sites which is comparable with the reported value of $\lambda \approx 17.0$ for *trans*-polyacetylene,[29] and the theoretically calculated $\lambda \approx 12$ for halogen-bridged CDW complexes.[19–21]

Table 2. Spin-Soliton Diffusion Rates D^* and Delocalization Lengths λ in a 1-D CDW Complex, [Pd(chxn)$_2$]-[PdBr$_2$(chxn)$_2$]Br$_4$ (**3**)

T/K	D^*/rad s^{-1} (uncertainty)	λ (uncertainty)
303	2×10^{13} ($1 < D^*/10^{13}$ rad s^{-1} < 4)	6 ($0 \le \lambda < 32$)
198	9×10^{11} ($6 < D^*/10^{11}$ rad s^{-1} < 14)	26 ($3 < \lambda < 35$)
125	6×10^{10} ($5 < D^*/10^{10}$ rad s^{-1} < 8)	20 ($\pm$ 2)

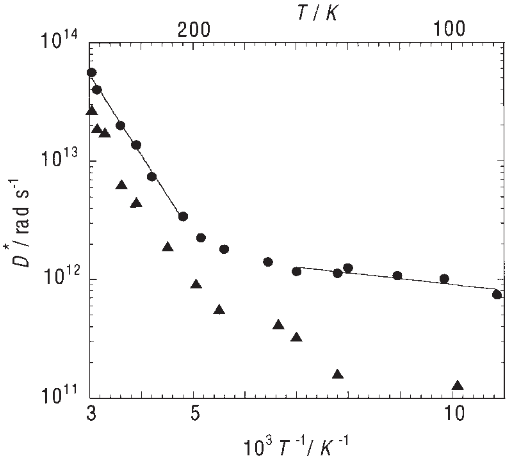

Fig. 16. Temperature dependences of the 1-D electron spin-diffusion rate D^* determined in [Pd(chxn)$_2$]-[PdBr$_2$(chxn)$_2$]Br$_4$ (**3**) at Larmor frequencies of 60 (●) and 30 (▲) MHz. Slopes of solid lines afford activation energies of the electron-spin diffusion.

The observed T_{1S} shown in Fig. 14 giving a minimum at ca. 200 K suggests the contributions from two mechanisms that are explainable by Eq. 1. In the low-temperature range, the spectrum density $f_{1D}(\omega_H)$ decreases upon heating, because D^* increases with temperature as seen from Eq. 2, while $kT\chi_S$ is expected to increase because TA-spins are thermally activated upon heating. In case the TA-spin increase is more effective than that in $f_{1D}(\omega_H)$, the resultant T_{1S} decreases upon heating. With increasing temperature, the number of TA-spins created seems to become gradually the saturated value. Since $f_{1D}(\omega_H)$ and $f_{1D}(\omega_e)$ decrease by the increase of D^* with temperature, this contribution in Eq. 1 becomes dominant in T_{1S}, resulting in the T_{1S} increase on heating in the high-temperature range.

A rough estimation of the diffusion rate D^* at a given magnetic field can be done by applying Eq. 6, if numerical values of χ_S, d_{TA}, and λ are available. By using d_{TA} as given above, χ_S derived from Eq. 8, and assuming $\lambda \approx 20$ as obtained at 125 K, D^* values were obtained from observed T_{1S} data in Fig. 14. Figure 16 shows determined temperature dependences of D^* at Larmor frequencies of 60.0 and 30.0 MHz. Above and below ca. 200 K, different temperature dependences were obtained but both could be expressed as the Arrhenius equation. From slopes of temperature dependences of D^* determined at 60.0 MHz, E_a values were obtained as $E_a \approx 140$ meV above ca. 200 K, and $E_a \approx 10.0$ meV below ca. 200 K. This E_a obtained above 200 K agrees well with 140 meV derived from the electrical conductivity measurement,[30] and the low-temperature E_a is close to $\Delta = 32$ meV determined from the temperature dependence of the spin susceptibility obtained from the ESR study.[8] The fact that the E_a below 200 K is low and comparable to those in complexes **1** and **2** given in Table 1 supports the claim that the neutral soliton is the main origin of the ^{1}H relaxation in **3** at low temperatures.

Above ca. 200 K, it is noted that another diffusion process with a high activation energy contributes to the relaxation. This high energy of 140 meV seems to be unacceptable for the neutral soliton. We can attribute this process to the migration of polarons which accompanies electrical conduction, because complex **3** shows electrical conductivities[30] much higher than those in **1** and **2**, as shown in Table 1, and also the activation energies from the conductivity and the present NMR measurements agree well as written above.

The present results in **3** were compared in Table 1 with analogous results obtained in **1** and **2** and *trans*-polyacetylene.[29] The diffusion rates of spin solitons are analogous with each other with an exception of **3**, which gave a smaller D^* value. This difference is explainable by the formation of the 2-D hydrogen bond in **3**, while almost the isolated 1-D chain structure remaining in **1** and **2**. This 2-D interaction between chains is expected to suppress the soliton migration, which can take place much more easily in **1** and **2** with the 1-D structure.

4.2 Spin-State in High-Purity Crystals of a CDW Complex, [Pd(chxn)$_2$][PdBr$_2$(chxn)$_2$]Br$_4$ Containing Lower Amounts of Impurities. The present complex **3**, [Pd(chxn)$_2$][PdBr$_2$(chxn)$_2$]Br$_4$ has been shown to be a suitable system to investigate dynamic properties of solitons and polarons, because a high concentration of paramagnetic M^{3+} sites compared with those in the other halogen-bridged CDW complexes can be formed in crystals. An interesting problem is whether these paramagnetic sites are intrinsic or are impurities in this complex. Recently, a new method for the preparation of high quality single crystals of halogen-bridged complexes was developed by using the electrochemical oxidation reaction.[31] With this method, large single crystals of **3** (expressed as **3-2**) were slowly grown over several months by controlling the electric current. Measurements by using these single crystals are expected to diminish effects from lattice imperfections and chain ends where most of impurities including paramagnetic metal sites seem to be concentrated.

ESR spectra observed for single crystals of **3-2** gave almost the same line-shape as that in the crystals (**3-1**) previously prepared by the Br$_2$ diffusion method,[32] but the signal intensity in **3-2** was much weaker than that in **3-1**.[33] The spin density in **3-2** derived from the spectrum intensity was ca. 1/10 compared with that in **3-1**, implying a much lower concentration of paramagnetic Pd^{3+} sites in **3-2**.

In Fig. 17, Arrhenius plots of ^{1}H T_1 (the short T_1 component) observed in **3-2** together with those in **3-1** are shown. Below 200 K, **3-2** gave T_1 values of several times longer than those in **3-1**, in good agreement with a low concentration of paramagnetic Pd^{3+} sites expected in **3-2**, in which the fluctuation of magnetic field at protons should be much weaker than that in **3-1**. Since almost the same temperature gradient was observed in **3-2** and in **3-1** in this temperature range, the same relaxation mechanism, i.e., the magnetic dipolar interactions between protons and rapidly diffusing neutral solitons[18] works in both samples, but of course less effectively in **3-2**. Above ca. 200 K, a small increase in T_1 upon heating was obtained in **3-2**, where an analogous marked T_1 increase was also observed in **3-1**.[18] This T_1 increase in both samples can be explained by the increase in the diffusion rate (D^*) of neutral solitons and polarons, as already discussed in Sec. 4.1. It is interesting that, on further heating of both **3-1** and **3-2**, T_1 values again showed a tendency to decrease. This mechanism is not clear in the present stage, but since the decrease in D^* upon heating was observed in **1** and **2** as discussed in Sec. 2, this T_1 decrease seems to be explained by using Eq. 6, where the decrease in D^* was attributed to thermal phonons which suppress the diffusion of solitons and polarons at high temperatures near the phase transitions in **1** and **2**.

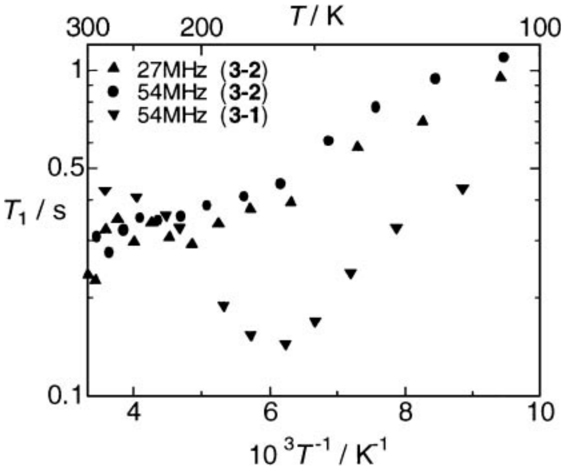

Fig. 17. Temparature dependences of ^{1}H T_1 observed in [Pd(chxn)$_2$][PdBr$_2$(chxn)$_2$]Br$_4$ prepared by the electrochemical oxidation method (**3-2**) and the Br$_2$ diffusion method (**3-1**).

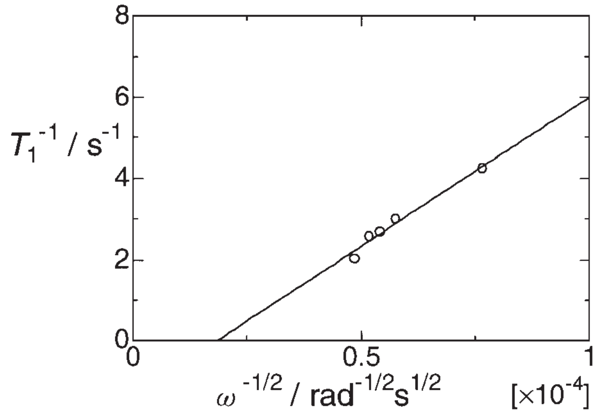

Fig. 18. A Larmor-frequency (ω) dependence of ^{1}H T_1 observed in [Pd(chxn)$_2$][PdBr$_2$(chxn)$_2$]Br$_4$ (**3-2**) prepared by the electrochemical oxidation method. The solid line was fitted by Eq. 6 in text.

Figure 18 shows a Larmor-frequency dependence of ^{1}H T_1 observed in **3-2** at 298 K. Since this result can be explained well by Eq. 6, the observed T_1 can be attributed to the 1-D diffusion of Pd^{3+} sites. It is noted that the D^* value evaluated from Eq. 6 using the slope in Fig. 18 became 10^{11} rad s^{-1}. This D^* is ca. 1/100 compared with that in **3-1** determined in the same temperature range. As shown in Fig. 16 and the discussion in Sec. 4.1, the origin of evaluated D^* in **3-1** was separated into two processes below and above ca. 200 K, mainly from neutral solitons and from polarons, respectively. If we consider the fact that the obtained D^* in **3-2** is close to those of neutral solitons determined below 200 K shown in Fig. 16, it is probable that the concentration of polarons is low in **3-2** at room temperature because of the high purity of **3-2**, and that the obtained D^* is mostly from neutral solitons.

From the above discussions on **3-1** and **3-2** containing different concentrations of lattice imperfections, it can be concluded that the formation of paramagnetic Pd^{3+} sites in this complex is mostly not intrinsic but depends on various kinds of imperfections, including the effect of chain ends. Because of the low energy difference between d_{z^2} orbitals in Pd^{2+} and Pd^{4+}, two neighboring Pd^{3+} sites seem to be formed at imperfect lattice sites such as impurities, defects, dislocations, and chain ends, which should be unstable and more active than the normal 1-D lattice.

5. Averaged-Valence (Mott–Hubbard) Complexes, $[NiX(chxn)_2]X_2$ (X: Cl, Br)

5.1 Chain-Structures Determined by Solid-State ^{13}C CP/MAS NMR. The X-ray diffraction study on $[NiX(chxn)_2]X_2$ (X: Cl (**6**), Br (**7**))[7,34] has shown that the bridging halogen atoms in –X–Ni–X–Ni–X– chains are located at the midpoint between neighboring Ni atoms as shown in Fig. 19. This structure is in contrast with that in foregoing CDW complexes. It can be expected from this result that all Ni atoms are equivalent with no Peierls distortion, and that this complex is in a so-called *Mott–Hubbard* state. This suggests that a paramagnetic 1-D chain is formed. In this section, studies on the Ni valence state in **6** and **7** using the solid-state CP/MAS (cross-polarization/magic-angle-spinning) ^{13}C NMR measurements are introduced; this technique can provide detailed information on the local magnetic structure in these 1-D complexes.

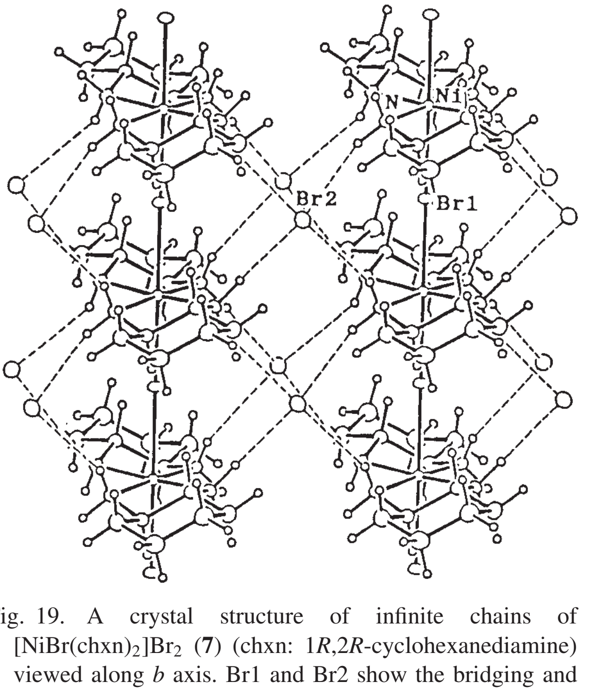

Fig. 19. A crystal structure of infinite chains of $[NiBr(chxn)_2]Br_2$ (**7**) (chxn: 1*R*,2*R*-cyclohexanediamine) viewed along *b* axis. Br1 and Br2 show the bridging and the counter Br ions, respectively. Br1 is located at the mid-point between two neighboring Ni atoms. Dashed lines exhibit hydrogen bonds (Ref. 7).

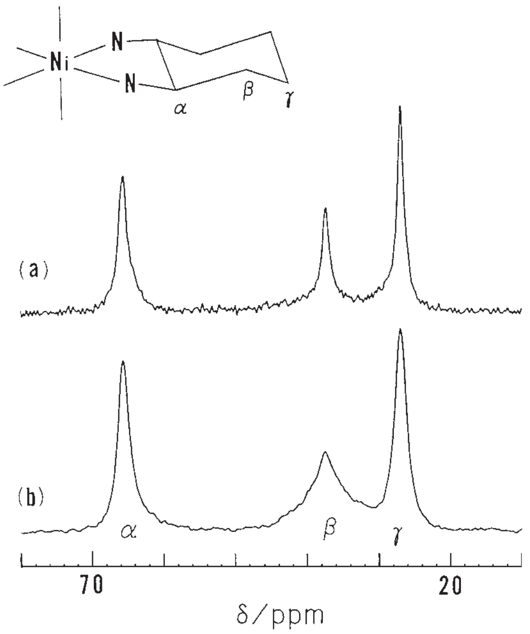

Fig. 20. CP-MAS ^{13}C NMR spectra in $[NiX(chxn)_2]X_2$ observed at room temperature, (a) X = Cl and (b) X = Br. α, β, and γ denote carbon positions in a cyclohexane ring (Ref. 35).

From ^{13}C NMR spectra consisting of three resonance lines in both **6** and **7**, observed at room temperature as shown in Fig. 20,[35] the presence of three kinds of nonequivalent carbons in crystals were shown. These results are in good agreement with the crystal structures,[7,34] in which all ligand cyclohexane molecules in crystals are crystallographically equivalent, implying the presence of three kinds of nonequivalent carbons, i.e., α, β, and γ carbons in a cyclohexane ring as shown in Fig. 20. The observed three lines were assigned from the low to the high field to be α-, β-, and γ-carbons in the ring.[36] For comparison, ^{13}C NMR spectra observed at room temperature in CDW Pd complexes with cyclohexanediamine (chxn) and ethylendiamine (en) ligands, together with a monomer complex $[Pd^{II}(chxn)_2]Cl_2$, are shown in Fig. 21. Observed chemical-shift values are summarized in Table 3.[35]

A marked difference between spectra in the present Ni complexes and in CDW complexes is that the α-carbon signal was a doublet in CDW complexes, whereas it was a sharp singlet in **6** and **7**. This result indicates that all Ni atoms in 1-D chains are magnetically equivalent in the NMR observation. X-ray diffraction studies[7,34] also reported that all Ni atoms are at the same distance from bridging halogens. From these results, Ni atoms are expected to be paramagnetic Ni^{3+}, and **6** and **7** form an $S = 1/2$ 1-D chain markedly different from the diamagnetic CDW state as observed in many Pt and Pd halogen-bridged complexes reported so far.

It has been reported that ^{13}C NMR signals in paramagnetic complexes in most cases afford marked chemical shifts, so-called paramagnetic or contact shifts,[37] and also broadened spectra. In the present complexes, however, chemical shifts at all carbon sites were shown to be close to values at correspond-

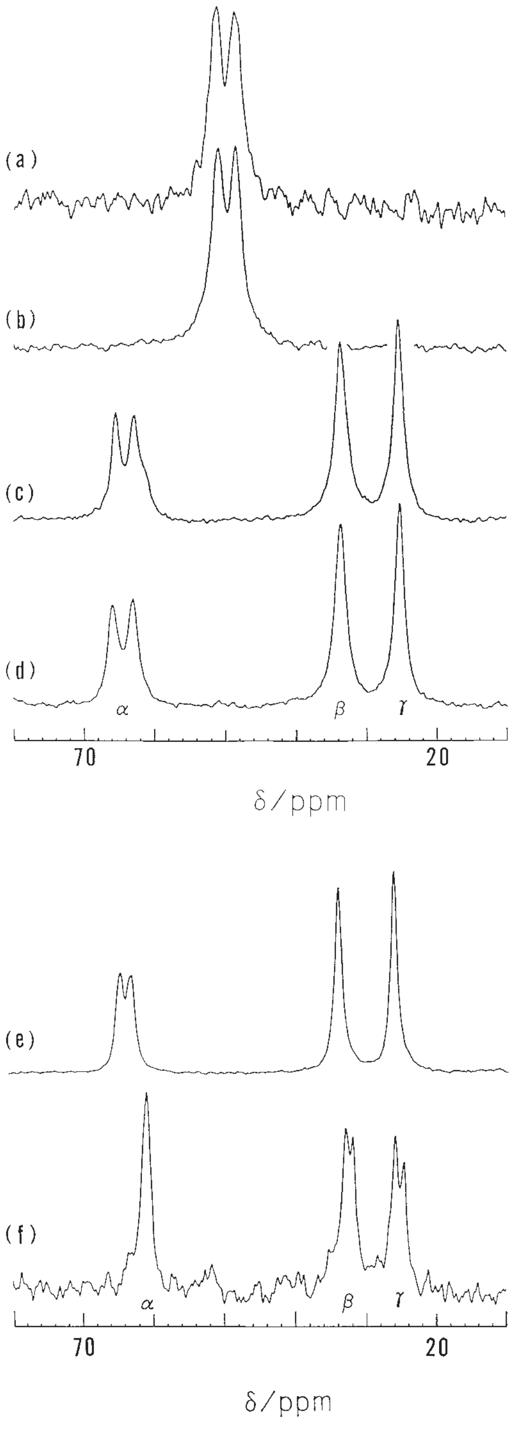

Fig. 21. CP-MAS ^{13}C NMR spectra of $[Pd(en)_2][PdX_2(en)_2](ClO_4)_4$ observed at room temperature, (a) X = Cl, (b) X = Br, $[Pd(chxn)_2][PdX_2(chxn)_2](ClO_4)_4$ (c) X = Cl, (d) X = Br, (e) $[Pd(chxn)_2][PdCl_2(chxn)_2]Cl_4$, and (f) $[Pd(chxn)_2]Cl_2$ (monomer complex). α, β, and γ are carbon positions in a cyclohexane ring shown in Fig. 20 (Ref. 35).

ing positions in the diamagnetic Pd complexes, and no marked signal-broadening was observed. These results imply that the paramagnetic interaction at these carbon sites is quite weak. The small shift values observed suggest low spin densities at the α-carbon owing to the marked decrease of the spin density in the σ-bond system. It can, accordingly, be expected that a strongly spin-coupled SDW state is formed in **6** and **7**.

5.2 ^{1}H NMR Relaxation Studies on Paramagnetic 1-D Ni^{3+} Spins. From the above analysis of ^{13}C NMR spectra, the formation of SDW 1-D chains of Ni^{3+} is expected in **6** and **7**. Since the NMR relaxation measurement is quite a sensitive probe to detect paramagnetic spins, the ^{1}H NMR relaxation time (T_1) measurements in **6** and **7** were carried out to determine whether $S = 1/2$ 1-D chains are formed or not. Observed ^{1}H T_1 values were almost independent of the Larmor frequency down to 100 K, and became ca. 250 ± 20 and 750 ± 100 ms in **6** and **7**, respectively. These values are quite short compared with $T_1 = 10$–100 s in corresponding diamagnetic CDW Pt and Pd complexes, $[M(chxn)_2][MX_2(chxn)_2]X_4$ (M: Pt, Pd; X: Cl, Br).[38] The observed short T_1 in the Ni complexes can be explained by the relaxation from paramagnetic Ni^{3+}. However, these T_1 values in **6** and **7** are too long as for T_1 in paramagnetic systems with a high density of unpaired electrons. This is because solid systems consisting of isolated paramagnetic ions or molecules usually afford short T_1 less than 1 ms[39] owing to strong fluctuations of the magnetic field made by isolated spins. These facts suggest the presence of a strong coupling between neighboring paramagnetic spins, which results in the suppressed fluctuation of the magnetic field made by unpaired spins.

From the above NMR results, complexes **6** and **7** are expected to form an $S = 1/2$ 1-D antiferromagnetic spin system. The magnetic susceptibility of **7** was measured and analyzed by the Bonner–Fisher model[40] of an antiferromagnetically coupled 1-D system. From obtained results, the presence of quite a large exchange interaction energy (J) amounting to ca. 3,600 K[8] was suggested. Since such a large J value is difficult to determine from susceptibility data observed in the low-temperature range up to 300 K, the presence of the strong interaction has not been concluded. In case this J value is acceptable, this system will be the 1-D system having the strongest antiferromagnetic interaction so far reported.

Recently, 1-D systems consisting of $S = 1/2$ paramagnetic spins with antiferromagnetic interactions have been intensively studied, because marked quantum effects are expected at low temperatures. It was shown that the ground state is quite different from the Néel state, which consists of one-dimensionally arranged anti-parallel spin vectors. Quantum mechanically, the $S = 1/2$ 1-D chain cannot form any state with a long-range order even at 0 K, but it has a fluctuated spin state of the quantum mechanical origin. This theoretical prediction is interesting, because a non-vanishing NMR spin-lattice relaxation rate is expected in the limit of the low temperature.[41] Sachdev[42] theoretically treated the fluctuation of the magnetic field in an $S = 1/2$ spin system with the Heisenberg-type interaction. When the exchange interaction is expressed as

$$H_{ex} = 2J\Sigma \boldsymbol{S}_i \cdot \boldsymbol{S}_{i+1}, \tag{11}$$

he proposed that the NMR spin-lattice relaxation time T_1 in the range of $T/J < 0.5$ can be written as

$$T_1{}^{-1} \propto \ln^{1/2}(2J/T). \tag{12}$$

To confirm that this prediction is acceptable, the measurement of ^{1}H T_1 was performed at low temperatures in a bromine-

Table 3. ^{13}C NMR Chemical Shifts (ppm) and Splitting Widths ($\Delta\nu$/ppm) of Doublet Lines Observed in Ethylenediamine (en) and at α-, β-, γ-Carbons in 1*R*,2*R*-Cyclohexanediamine (chxn) Ligands in Halogen-Bridged 1-D Complexes of Pd and Ni, Together with a Monomer Complex $[Pd(chxn)_2]Cl_2$

Complex	Position			
	α	$\Delta\nu$	β	γ
$[NiCl(chxn)_2]Cl_2$	65.4		37.3	26.8
$[NiBr(chxn)_2]Br_2$	65.5		37.4	26.8
$[Pd(chxn)_2][PdCl_2(chxn)_2]Cl_4$	62.7	1.4	33.8	26.0
	64.1			
$[Pd(chxn)_2][PdCl_2(chxn)_2](ClO_4)_4$	62.8	2.6	33.6	25.4
	65.4			
$[Pd(chxn)_2][PdBr_2(chxn)_2](ClO_4)_4$	62.9	2.7	33.6	25.3
	65.6			
$[Pd(en)_2][PdCl_2(en)_2](ClO_4)_4$	48.6	2.5		
	51.1			
$[Pd(en)_2][PdBr_2(en)_2](ClO_4)_4$	48.5	2.4		
	50.9			
$[Pd(chxn)_2]Cl_2$	61.0		33.0	25.9
			32.0	24.7

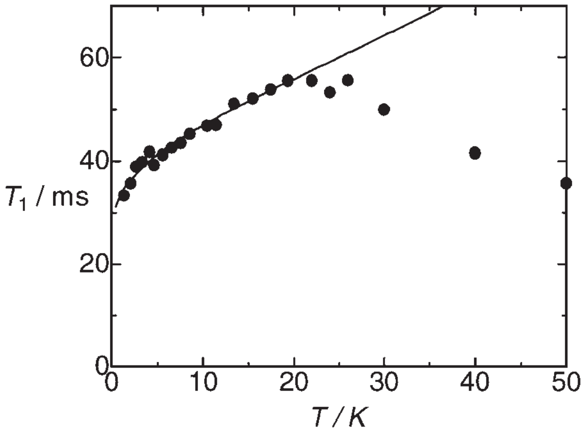

Fig. 22. A temperature dependence of ^{1}H NMR spin-lattice relaxation time (T_1) observed in $[CuBr_2(AdeH^+)_2]Br_2$ (Ad: adenine) at low-temperatures. The solid line is theoretically calculated using the Sachdev's treatment (see text).

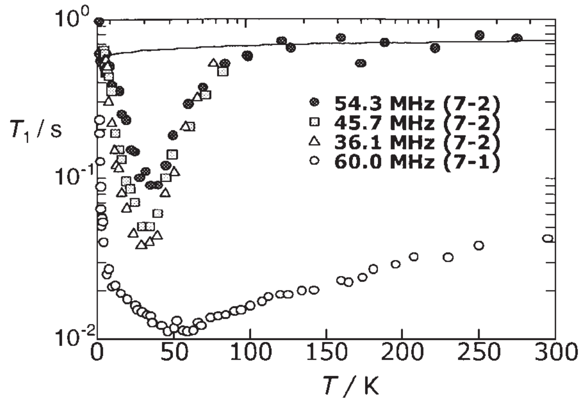

Fig. 23. Temperature dependences of ^{1}H NMR spin-lattice relaxation time (T_1) observed in $[NiBr(chxn)_2]Br_2$ prepared by the Br_2-diffusion (**7-1**) and the electrochemical method (**7-2**). The solid line is theoretically calculated by the Sachdev's treatment (see text).

bridged 1-D chain complex $[CuBr_2(AdH^+)_2]Br_2$ (Ad: adenine)[43] that has been determined to be an antiferromagnetically coupled $S = 1/2$ 1-D system with $J = 52.6$ K.[44] ^{1}H T_1 values observed in the low-temperature range are shown in Fig. 22. T_1 became short with decreasing temperature below 25 K and looked to approach a finite value in the limit of the low temperature, as theoretically predicted. When the reported J value is used, a theoretical temperature-dependent T_1 curve could be evaluated as shown in Fig. 22, reproducing well the experimental result below ca. 20 K.

Here, the magnetic structure and the dynamic electron-spin behavior of 1-D chains in **7** were studied to obtain the information about magnetic interactions that were expected to be quite strong by measuring the temperature dependence of the ^{1}H NMR T_1 in the low-temperature range; the obtained data are discussed in connection with the above relaxation theory.

For samples of the NMR measurement, two kinds of crystals prepared by two different methods which gave a marked difference were used. As the first method, a polymer complex **7** was obtained by the oxidation of the monomer complex $[Ni^{II}(chxn)_2]Br_2$ by slowly diffusing Br_2 gas into the solution.[7] Fine plate crystals were obtained in a week. As the other method, a recently developed electrochemical-oxidation technique was used,[31] and several mm size single crystals were obtained in 2–3 months. The crystals prepared by the 1st and the 2nd methods are hereafter named **7-1** and **7-2**, respectively; they were confirmed to have the same crystal structure at room temperature.

The ^{1}H magnetization recovery in the NMR relaxation measurement showed a non-exponential decay in both samples. The short T_1 component was major and 60–90% of the ^{1}H magnetization in the whole temperature range studied.

In the first step, ^{1}H T_1 in **7-1** was measured and the T_1 of the short component observed is shown in Fig. 23. It is noted that a T_1 expansion was obtained upon cooling to 1.8 K. This result was inconsistent with the above theoretical prediction by Sachdev.[42]

A quite different relaxation behavior from that in **7-1** was obtained in **7-2**, as shown in Fig. 23, where **7-2** gave ca. 10 times longer T_1 values in the whole temperature range studied and no marked T_1 expansion was found below 4.2 K. A possible reason why the short T_1 was obtained in **7-1** is the presence of paramagnetic impurities contained as lattice imperfections and in chain ends which are expected more in **7-1** because of much smaller crystal sizes and a shorter crystal-growing time. Since the presence of two relaxation mechanisms is expected below and above ca. 80 K in **7-2** as seen in Fig. 23, T_1 data were divided into two components, i.e., the almost temperature independent high-temperature part and the minimum observed at ca. 30 K. The theoretical T_1 values given in Eq. 12, which was fitted to the data observed in the high-temperature range is shown in Fig. 23. From the fitting, the exchange interaction energy of $J = 2500 \pm 1000$ K was evaluated. This value is comparable to 2700 ± 500 K estimated from spin susceptibility data obtained by the ESR measurement[45] and also a recently reported value of 1700 K derived from the Bonner–Fisher fitting of the magnetic susceptibility.[46] It is noteworthy that these J values are almost the same as 2200 K in Sr_2CuO_3[47] that has been reported to be the antiferromagnetically coupled 1-D system having the highest J value so far reported.

The other relaxation mechanism giving a frequency dependent T_1 minimum at ca. 30 K is attributable to some dynamic processes giving fluctuations of the magnetic field. The short ^1H T_1 minimum value observed at low temperatures cannot be attributed to lattice motions,[48] but can be due to the fluctuation of electron-spins.

In a preliminary study in our group, an ^{81}Br NQR measurement in **7-2** afforded a single resonance line at room temperature, in agreement with the averaged-valence-structure in this complex. Upon cooling, two symmetrically split lines were observed below ca. 40 K, indicating the onset of a phase transition. The fact that this temperature agrees with that in the ^1H T_1 anomaly suggests the onset of some changes of the spin structure in the low-temperature range.

It is noted that T_1 values observed in the low-temperature limit were longer than values calculated using Eq. 12 as shown in Fig. 23. This T_1 increase observed at low temperatures suggests that some mechanism suppressing the spin fluctuation contributes to the relaxation.

6. Spin Structures in Mixed-Metal 1-D Halogen-Bridged Complexes $[Ni_{1-x}Pd_xX(chxn)_2]X_2$ $(0.0 \le x \le 1.0$, X: Cl, Br)

Halogen-bridged complexes $[MX(chxn)_2]X_2$ form a diamagnetic CDW state expressed as $–X–M^{2+}–X–M^{4+}–$ for M = Pd,[49] while a paramagnetic Mott–Hubbard state as $–X–M^{3+}–X–M^{3+}–$ for M = Ni.[7] It is noteworthy that both Pd and Ni complexes crystallize in the same structure (*I*222), because, in the Pd complex, coordinates of bridging Br atoms are disordered between two positions on the 1-D chain when observed by the X-ray diffraction. Recently, crystals of mixed-metal complexes $[Ni_{1-x}Pd_xX(chxn)_2]X_2$, were prepared by the electrochemical oxidation technique.[50] It was shown that these complexes crystallize in a homogeneously mixed lattice of the two kinds of metals with the structure (*I*222), isomorphous with those of the single metal complexes. X-ray diffraction studies[50] on Br-bridged complexes over the whole range $0.0 \le x \le 1.0$ gave a continuous change of the lattice constant from $b = 51.67$ nm in $x = 0.0$ to 52.92 nm in $x = 1.0$. The x dependence of ESR spectra[51] also revealed a continuous variation of the spectrum-width with x. A characteristic change in the spin susceptibility was observed in a range $0.0 < x < 0.6$, where the susceptibility showed no linear relation with x, but an almost constant value up to $x \sim 0.6$, then sharply decreased to $x = 1.0$ with increasing x. It is expected from this result that most of diamagnetic Pd sites behave as if they are paramagnetic at concentrations lower than $x \sim 0.6$. Similar behavior was also observed in N–H stretching bands in Pd^{2+} and Pd^{4+} units in IR spectra,[50] which showed a gradual shift to that in the Ni^{3+} unit with decreasing x. An analogous shift was also observed[50] in the Pd–Br stretching band of the Raman scattering measurement.

These studies allow us to expect instability and fluctuations of the Pd valence state in the mixed-metal 1-D system. The valence change to paramagnetic Pd^{3+} from diamagnetic Pd^{2+}, Pd^{4+} seems to take place, because the energy difference between Pd^{2+} and Pd^{4+} is small[8] compared with the other kinds of CDW halogen-bridged complexes of Pd and Pt.

By measuring ^{13}C NMR spectra, one can obtain information on local magnetic structures and magnetic field fluctuations on ligand carbons. In this section, ^{13}C magic-angle-spinning (MAS) NMR spectra and the ^1H NMR relaxation in $[Ni_{1-x}Pd_xX(chxn)_2]X_2$ (X: Cl, Br; $0.0 \le x \le 1.0$) are presented and the local electronic structure in mixed-metal 1-D chains is discussed.[52]

^{13}C MAS NMR spectra for $[Ni_{1-x}Pd_xCl(chxn)_2]Cl_2$ and $[Ni_{1-x}Pd_xBr(chxn)_2]Br_2$ in a range $0.0 \le x \le 1.0$ observed at room temperature are shown in Figs. 24 and 25, respectively. Three kinds of carbons C_α, C_β, and C_γ in a chxn (1*R*,2*R*-cyclohexanediamine) ligand were observed as separated peaks in both systems. A doublet signal of the C_α carbon observed at $x = 1.0$ can be assigned to Pd^{2+} and Pd^{4+} sites, and a single C_α line at $x = 0.0$ indicates the averaged Ni^{3+} state.[35] In both Cl and Br complexes, the fact that the C_α and C_β signals keep the same shift values with increasing x from 0.0 suggests that Ni atoms are always in the trivalent state regardless of the Pd

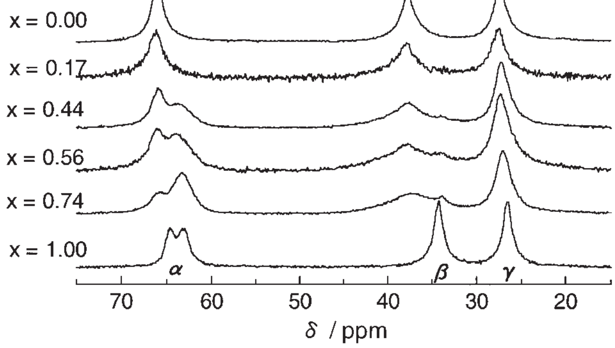

Fig. 24. ^{13}C MAS NMR spectra observed at room temperature in $[Ni_{1-x}Pd_xCl(chxn)_2]Cl_3$ in the range $0.0 \le x \le 1.0$ and carbon positions in a cyclohexanediamine ligand.

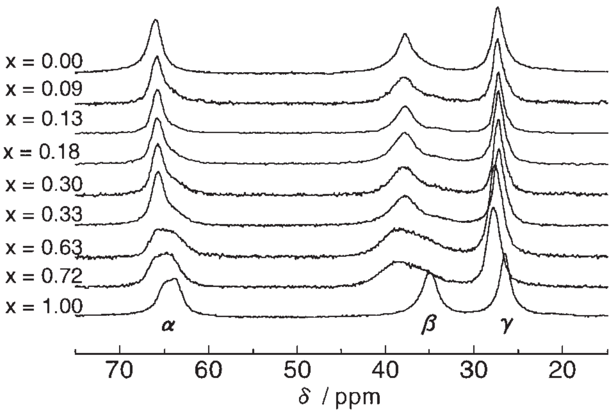

Fig. 25. ^{13}C MAS NMR spectra observed at room temperature in $[Ni_{1-x}Pd_xBr(chxn)_2]Br_2$ in the range $0.0 \leq x \leq 1.0$.

concentration. On the contrary, C_α and C_β signals in $x = 1.0$ became weak and broad with decreasing x. A clear doublet observed at $x = 1.0$ corresponding to Pd^{2+} and Pd^{4+} sites was broadened into a single peak on introducing even small amounts of Ni. This indicates that the valencies of Pd^{2+} and Pd^{4+} become unstable even for a small quantity of Ni^{3+}. An analogous spectrum change was also observed for the C_β site, where the signal showed a rapid broadening with decreasing x from 1.0, indicating a rapid increase in the line-width with the mixing of Ni^{3+}.

C_α signals observed in the mixed metal range in the Cl complex were separated into two components, corresponding to Ni and Pd sites. Obtained shifts and broadenings in the spectra of Pd carbons suggest the fluctuation of Pd^{2+} and Pd^{4+} valences attributable to the mixing of the paramagnetic Pd^{3+} state. This explanation agrees well with the spin susceptibility data obtained from ESR measurements of the Br complex[51] that reported the formation of paramagnetic Pd^{3+} sites in the presence of Ni^{3+} in $x < 0.6$. The present NMR data suggest that the unstable Pd valency can be seen even in the much low Ni concentration range of $x > 0.7$.

An analogous discussion can be made for the Br complex shown in Fig. 25. The fact that the spectrum splitting in the C_α signal for $x = 1.0$ is unclear implies that the valence mixing in Pd is easier than that in the Cl system, because the energy difference between Pd^{2+} and Pd^{4+} is expected to be much smaller than that in the Cl complex. In fact, the spectrum broadening at C_α and C_β observed with decreasing x was significant compared with those in Cl complexes. Quite analogous results were derived from Raman spectra,[50] which afforded a gradual decrease of the intensity in the Pd–Br stretching band with decreasing x. This was explained by the Pd valence fluctuation caused by mixing Ni^{3+}.

A more sensitive detection of the valence instability in this mixed-metal system was carried out by measuring the ^{1}H NMR spin-lattice relaxation time T_1. At $x = 1.0$, a gradual decrease in T_1 observed upon heating from ca. 100 K was explained by the formation of spin solitons from impurity amounts of Pd^{3+}, as described in Sec. 4. With a little reduction of x from 1.0, T_1 values of the same order of ca. 1 s as in the complex of $x = 1.0$ was obtained. This result is quite unusual and is inconsistent with the general consideration that the relaxation becomes quite rapid when even small amounts of paramagnetic species are introduced in diamagnetic systems. Since the presence of the paramagnetic Ni^{3+} was confirmed even in a low mixing ratio by the ^{13}C spectrum analysis given above, the fluctuation of magnetic field made by almost isolated Ni spins should give a strong relaxation mechanism in ^{1}H T_1. The fact that mixed-metal complexes containing small amounts of paramagnetic Ni^{3+} gave a quite slow relaxation implies that the spin fluctuation in Ni^{3+} is suppressed by some strong interactions. The most probable mechanism is strong magnetic couplings of Ni^{3+} with nearest-neighboring paramagnetic Pd^{3+} sites formed from diamagnetic Pd^{2+} and Pd^{4+} sites in the 1-D chain.

The results in this section imply an easy formation of Pd^{3+} even at a low concentration of paramagnetic Ni^{3+} and support the fluctuation model of the Pd valency derived from ESR studies.[51]

7. Molecular Motions Associated with Phase Transitions in CDW 1-D Complexes

7.1 Order–Disorder Type Transitions in $[Pt(en)_2][PtX_2(en)_2](ClO_4)_4$ (X: I, Br). As described in Secs. 2 and 3, structural phase transitions were found in $[Pt(en)_2][PtX_2(en)_2](ClO_4)_4$ (X: I, Br) near room temperature.[15] It has been reported[15,53] that conformations of en chelate rings in the $M(en)_2$ moieties are transformed at the transition from δ–λ or λ–δ in the low-temperature phase($P2_1/m$) to λ–λ or δ–δ, respectively, in the high-temperature phase (*Ibam*). Crystal structures indicating differences in coformations of Pt(en) chelate rings in these two phases are shown in Fig. 26. A recently prepared new modification of $[Pt(en)_2][PtBr_2(en)_2](ClO_4)_4$ (**2**) obtained by the crystallization below the phase transition point ($T_{tr} = 299$ K), was shown to be different from the above crystals; it was monoclinic ($C2/m$) with disordered en conformations.[54] This structure is isomorphous with the high-temperature phase of $[Pt(en)_2][PtI_2(en)_2](ClO_4)_4$ (**8**), which was suggested[55] to transform into an ordered form ($C2/c$) in a range 150–160 K upon cooling.[56]

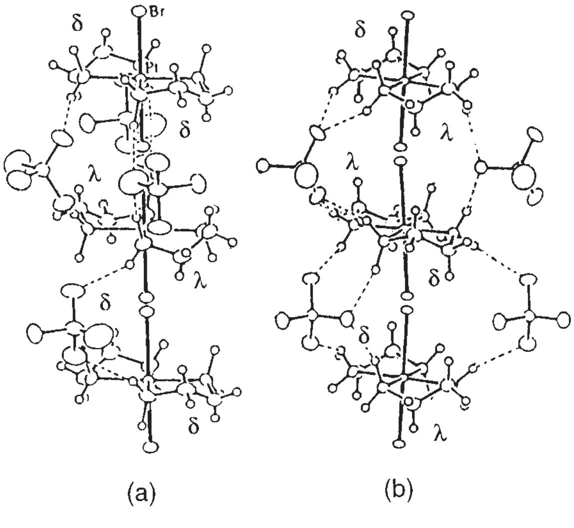

Fig. 26. Conformations (δ, λ) of Pt(en) chelate rings in (a) the high-temperature phase and (b) the low-temperature phase in $[Pt(en)_2][PtBr_2(en)_2](ClO_4)_4$ (**2**).

In this section, the phase transitions closely connected with the ethylendiamine conformation and molecular motions at the transitions in these crystals are discussed based on the thermal and ^{2}H NMR spectrum measurements, together with ^{1}H and ^{2}H spin-lattice relaxation studies.[57]

The presence of a phase transition in **8** was confirmed by observing a weak and broad heat anomaly with a peak at 157 ± 5 K, accompanied by a long tail, on the low-temperature side in the measurement of differential thermal analysis (DTA).[57] This temperature agrees well with T_{tr} of 150–160 K estimated from the neutron diffraction study.[56] Differential scanning calorometry (DSC) measurements showed that the recently reported new modification of **2** with the disordered en conformations is in a metastable state,[57] and transforms at 381 K upon heating into the stable form (*Ibam*) with the ordered conformations. The determined phase diagrams in **2** and **8** together with the hysteresis recorded on **2** are shown in Fig. 27.

^{2}H NMR spectra observed in partially deuterated [Pt(NH$_2$-(CD$_2$)$_2$NH$_2$)$_2$][PtI$_2$(NH$_2$(CD$_2$)$_2$NH$_2$)$_2$](ClO$_4$)$_4$ (**8-CD**) and [Pt(ND$_2$(CH$_2$)$_2$ND$_2$)$_2$][PtI$_2$(ND$_2$(CH$_2$)$_2$ND$_2$)$_2$](ClO$_4$)$_4$ (**8-ND**) are shown in Fig. 28.[57] ^{2}H Quadrupole coupling constants (qcc) and the asymmetry parameters (η) of the principal values of the electric field gradient (efg) tensors evaluated from observed spectra showed that almost rigid en ligands with fixed C–D and N–D directions[58] in crystals of both analogs at ca. 140 K begin to move upon heating. Spectrum changes in both

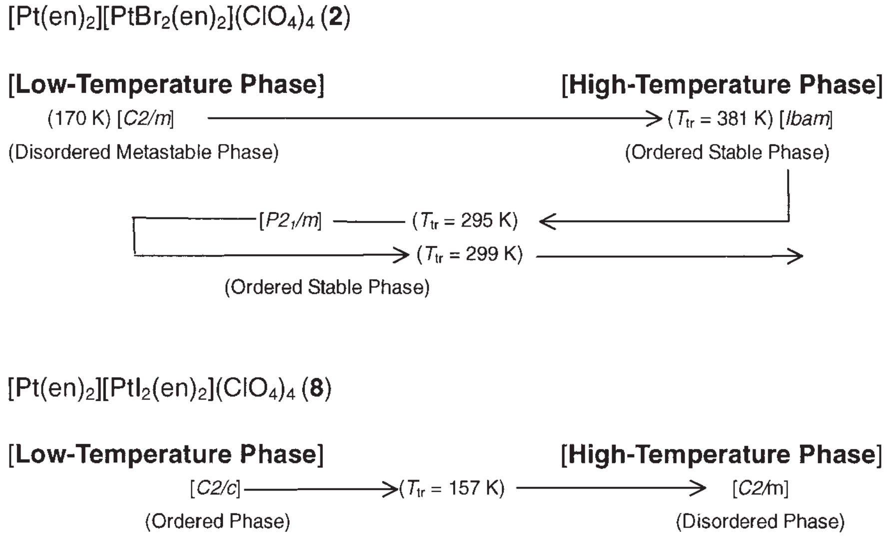

Fig. 27. Thermograms determined by the differential scanning calorimetry (DSC) measurement of [Pt(en)$_2$][PtBr$_2$(en)$_2$](ClO$_4$)$_4$ (**2**) and [Pt(en)$_2$][PtI$_2$(en)$_2$](ClO$_4$)$_4$ (**8**).

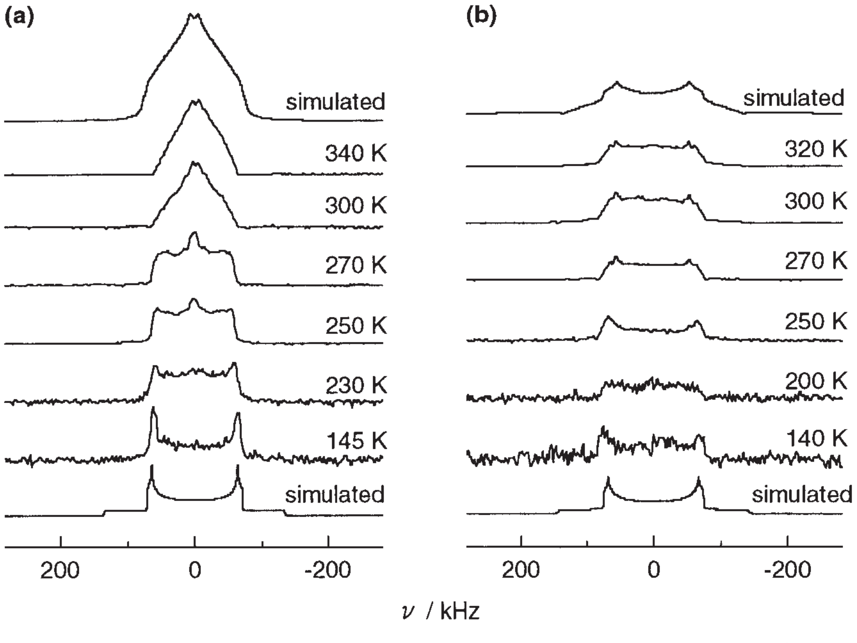

Fig. 28. ^{2}H NMR spectra observed in (a) [Pt(NH$_2$(CD$_2$)$_2$NH$_2$)$_2$][PtI$_2$(NH$_2$(CD$_2$)$_2$NH$_2$)$_2$](ClO$_4$) (**8-CD**) and (b) [Pt(ND$_2$(CH$_2$)$_2$-ND$_2$)$_2$][PtI$_2$(ND$_2$(CH$_2$)$_2$ND$_2$)$_2$](ClO$_4$) (**8-ND**). Top and bottom spectra are simulated for the highest- and lowest-temperature spectra observed, respectively.

analogs observed above room temperature imply the onset of two-site jumps of C–D and N–D bond directions,[59] consistent with the X-ray diffraction study of **8** that revealed the disordered conformations of en ligand in the high-temperature phase,[55] if the dynamic disorder model is assumed. This two-site jump is expected to take place between asymmetric potential wells from the analysis of ^{1}H NMR T_1 and the second moment (M_2) of absorptions given below. Using the potential well model shown in Fig. 29, and static e^2Qq and η values obtained in the low-temperature phase, ^{2}H NMR spectra were simulated for various jump angles 2θ and potential energy differences ΔE. Some examples of simulated spectra are shown in Fig. 30. The best-fitted 2θ and ΔE values at 300 K for C–D and N–D jumps are given in Table 4 together with parameters determined from ^{1}H NMR data given below.

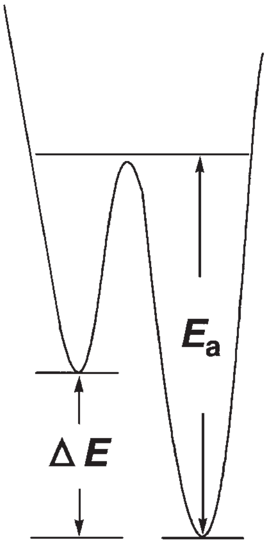

Fig. 29. A model of the asymmetric double-well potential.

Since jump angles due to the en conformational change between λ and δ forms were estimated to be ca. 60° and ca. 30° for C–D and N–D bond directions, respectively, using the structural data,[55] determined jump angles 68° and 30° for the C–D and N–D direction, respectively, can be explained by the onset of the conformational change in the M–en chelate ring. This motional model is consistent with results of X-ray and neutron diffractions[55,56] as well as with those of the present DSC study indicating the occurrence of an order–disorder type phase transition at 157 K associated with λ and δ conformations in the Pt(en) chelate ring.

In Fig. 31, temperature dependences of ^{1}H NMR spin-lattice relaxation times ($T_{1\mathrm{H}}$) observed in **8** and **2** in the metastable monoclinic phase, and the ^{2}H NMR relaxation time ($T_{1\mathrm{D}}$) in **8-CD** and **8-ND** are shown.[57] All minima observed at ca. 350 K for $T_{1\mathrm{H}}$ and $T_{1\mathrm{D}}$ are attributable to the puckering motion of the en chelate rings that accompanied the conformation change. As for the NMR relaxation, the BPP theory[60] has been widely applied for motional processes in molecular crystals. This theo-

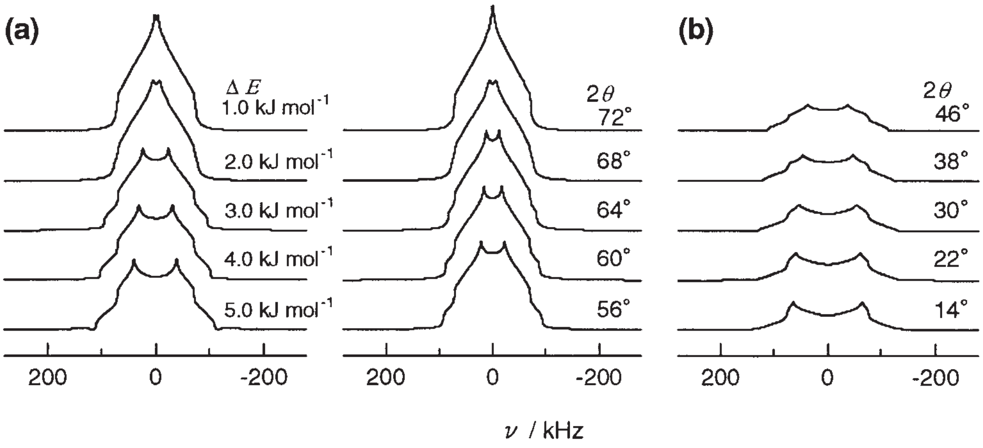

Fig. 30. ^{2}H NMR spectra simulated for (a) $[Pt(NH_2(CD_2)_2NH_2)_2][PtI_2(NH_2(CD_2)_2NH_2)_2](ClO_4)$ (**8-CD**) for various potential differences (ΔE) between two C–D jump directions for a jump angle of $2\theta = 68°$ (left), and various 2θ values for $\Delta E = 2.0$ kJ mol^{-1} (right), and (b) $[Pt(ND_2(CH_2)_2ND_2)_2][PtI_2(ND_2(CH_2)_2ND_2)_2](ClO_4)$ (**8-ND**) for $\Delta E = 2.0$ kJ mol^{-1}. All spectra were simulated at a jump rate of 10.0 MHz.

Table 4. Activation Energies (E_a), Potential Energy Differences (ΔE), Jump Angles of C–D and N–D Directions (2θ), Reductions of ^{1}H NMR Second Moments (ΔM_2) and Correlation Times at the Infinite Temperature (τ_0) of the Puckering Motion of Pt(en) Chelate Rings in Asymmetric Potential Wells in $[Pt(en)_2][PtI_2(en)_2](ClO_4)_4$ (**8**) and Its Partially Deuterated Analogs Containing CD_2 groups (**8-CD**) and ND_2 groups (**8-ND**), Together with $[Pt(en)_2][PtBr_2(en)_2](ClO_4)_4$ (**2**) Determined by ^{1}H and ^{2}H NMR Relaxation Studies

Compound	E_a/kJ mol^{-1}	ΔE/kJ mol^{-1}	2θ/degree	ΔM_2/mT^2	$\tau_0/10^{-14}$
$[Pt(NH_2(CH_2)_2NH_2)_2][PtI_2(H_2N(CH_2)_2NH_2)_2](ClO_4)_4$ (**8**)	31.0 ± 0.5	4.5 ± 1.0	—	0.12 ± 0.02	48 ± 0.5
$[Pt(NH_2(CD_2)_2NH_2)_2][PtI_2(H_2N(CD_2)_2NH_2)_2](ClO_4)_4$ (**8-CD**)	34.2 ± 0.5	2.9 ± 0.3 (2.0 ± 1.0)	65 ± 2 (68 ± 2)	—	8.0 ± 0.5
$[Pt(ND_2(CH_2)_2ND_2)_2][PtI_2(D_2N(CH_2)_2ND_2)_2](ClO_4)_4$ (**8-ND**)	34.8 ± 0.5	3.1 ± 0.5	28 ± 2 (30 ± 4)	—	8.2 ± 1.0
$[Pt(NH_2(CH_2)_2NH_2)_2][PtBr_2(H_2N(CH_2)_2NH_2)_2](ClO_4)_4$ (**2**)	31.0 ± 0.5	5.2 ± 0.5	—	0.12 ± 0.02	44 ± 1.0

Figures in parentheses are values obtained from ^{2}H spectrum analysis.

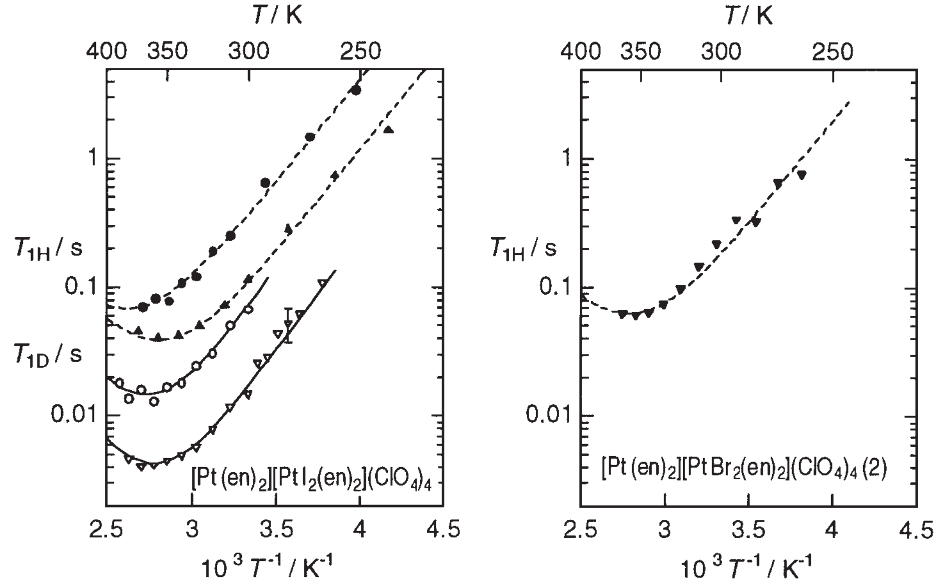

Fig. 31. ^{1}H NMR spin-lattice relaxation times (T_{1H}) observed in [Pt(en)$_2$][PtI$_2$(en)$_2$](ClO$_4$)$_4$ (**8**) at 29.0 (▲) and 54.3 MHz (●), [Pt(en)$_2$][PtBr$_2$(en)$_2$](ClO$_4$)$_4$ (**2**) at 54.3 MHz (▼) and ^{2}H NMR spin-lattice relaxation times (T_{1D}) in [Pt(NH$_2$(CD$_2$)$_2$NH$_2$)$_2$]-[PtI$_2$(NH$_2$(CD$_2$)$_2$NH$_2$)$_2$](ClO$_4$) (**8-CD**) (○) and [Pt(ND$_2$(CH$_2$)$_2$ND$_2$)$_2$][PtI$_2$(ND$_2$(CH$_2$)$_2$ND$_2$)$_2$](ClO$_4$) (**8-ND**) (▽) observed at 46.05 MHz. Broken and solid lines are the best-fitted theoretical values.

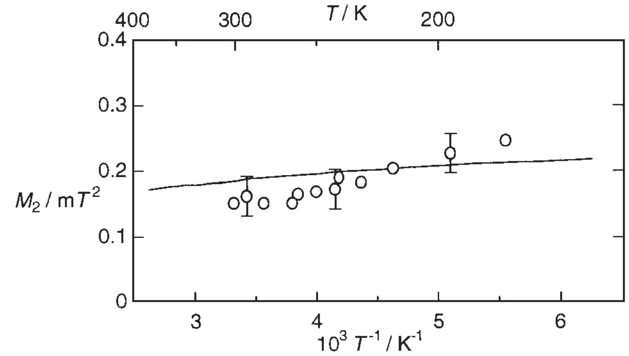

Fig. 32. A temperature dependence of second moments (M_2) of ^{1}H NMR absorptions in [Pt(en)$_2$][PtI$_2$(en)$_2$]-(ClO$_4$)$_4$ (**8**). The solid curve was calculated by the two-site-jump model in an asymmetric double-well potential.

ry requires a Larmor frequency (ω) dependence of T_1 given by $T_1{}^{-1} \propto \omega^2$ in the low-temperature side of the T_1 minimum. The observed ^{1}H T_1 in **8** shown in Fig. 31, however, disagrees with this prediction and roughly proportional to $\omega^{1.5}$. At the same time, as seen in Fig. 32, the temperature dependence of the second moment (M_2) of ^{1}H NMR absorptions observed in **8** showed an unusually gradual decrease from 0.22 to 0.15 mT^2 in a wide range of 200–300 K. This M_2 decrease can correspond to the gradual narrowing of ^{2}H NMR spectra by en motions observed in the same temperature range for **8-CD** and **8-ND**.

These anomalous T_1 and M_2 changes can be explained well by introducing a jumping model in an asymmetric double-well potential for the two conformations of en molecules in consistent with the ^{2}H NMR spectrum analysis given above. By assuming an unequal-two-well-potential model given in Fig. 29, the two-site jumps give T_{1H} due to the magnetic dipolar relaxation expressed as[61]

$$T_{1H}^{-1} = \frac{2}{3}\gamma_H^2 \Delta M_2 \frac{4a}{(1+a)^2}\left[\frac{\tau}{1+\omega^2\tau^2} + \frac{4\tau}{1+4\omega^2\tau^2}\right], \qquad (13)$$

where γ_H, τ, a, and ΔM_2 are the proton magnetogyric ratio, the correlation time of the motion, the population parameter, and the reduction of the M_2 value due to the onset of the motion, respectively. Here, a and τ are, respectively, given by

$$a = \exp\left(\frac{\Delta E}{RT}\right) \qquad (14)$$

and

$$\tau = \frac{1}{1+a}\tau_0 \exp\left(\frac{E_a}{RT}\right), \qquad (15)$$

where E_a and ΔE are the activation energy and the potential-energy difference, respectively, given in Fig. 29. These parameters were determined by fitting Eqs. 13–15 to the observed T_{1H} data in Fig. 31. The best-fitted theoretical values and the determined parameters are shown in Fig. 31 and Table 4, respectively.

^{1}H NMR M_2 values after the onset of the Pt(en)$_2$ chelate-ring motion were theoretically evaluated using the Van-Vleck equation[62] which afforded the following equation of the $M_2{}^{\text{mot}}$ for the two-site jumps of the H–H vector directions[63] given by

$$M_2{}^{\text{mot}}{}_{jk} = \frac{9}{20}\gamma_H^4 \hbar^2 \left[\frac{1}{r_{jkA}^6} + \frac{1}{r_{jkB}^6} + \frac{3\cos^2\theta_{jk} - 1}{r_{jkA}^3 r_{jkB}^3}\right]. \qquad (16)$$

Here, $M_2{}^{\text{mot}}{}_{jk}$ and r_{jkA}, r_{jkB} and θ_{jk} are the M_2 contributed from the motional-average dipolar interaction between the j-th and k-th protons, the inter-proton distance in A and B conformations and the two-site jump angle of the vector between j-th and k-th protons, respectively. The M_2 in the rigid lattice for **8** was determined to be $M_2{}^{\text{rig}} = 0.228 \pm 0.01$ mT^2 and $M_2{}^{\text{mot}}$ became 0.108 ± 0.005 mT^2. The difference of 0.120 mT^2 (ΔM_2) between these values agreed well with 0.12 ± 0.02 mT^2 obtained from the $T_{1\mathrm{H}}$ fitting given above.

^{2}H NMR $T_{1\mathrm{D}}$ temperature dependences observed in **8-CD** and **8-ND** in Fig. 31 were analyzed by[64]

$$T_{1\mathrm{D}}^{-1} = \frac{1}{10}\frac{4a}{(1+a)^2}\left(\frac{3\Delta e^2Qq_{\mathrm{rig}}}{4\hbar}\right)^2 \times \sin^2 2\theta\left[\frac{\tau_{\mathrm{D}}}{1+\omega_{\mathrm{D}}^2\tau_{\mathrm{D}}^2} + \frac{4\tau_{\mathrm{D}}}{1+4\omega_{\mathrm{D}}^2\tau_{\mathrm{D}}^2}\right], \qquad (17)$$

where $\Delta e^2Qq_{\mathrm{rig}}$, τ_{D}, and ω_{D} are the reduction of qcc in this motional process, the motional correlation time, and the ^{2}H angular NMR frequency, respectively. The best-fitted $T_{1\mathrm{D}}$ values determined by Eqs. 14, 15, and 17, are given in Fig. 31, and the obtained parameters are in Table 4. Determined $E_\mathrm{a} \approx 34.5$ and $\Delta E \approx 3$ kJ mol^{-1} agreed well with 31.0 and 4.5 kJ mol^{-1}, respectively, obtained by the $T_{1\mathrm{H}}$ fitting. Using these activation parameters and jump angles obtained from ^{2}H NMR spectra, high-temperature ^{2}H spectra were simulated and are shown in Fig. 28, giving good agreement with the observed spectra. The analogously fitted ^{1}H T_1 and parameters obtained for **2** in the metastable monoclinic phase are shown in Fig. 31 and Table 4, respectively. The fact that **2** gives a ΔE value larger than those in iodo complexes is explained by the stronger interactions between neighboring chelate rings in **2** due to its shorter Pt–Pt distance.

When the foregoing ^{2}H NMR spectra, ^{1}H and ^{2}H T_1 and ^{1}H M_2 analyses are combined, the disordered structure as for the en conformation in the high-temperature phase of **8** studied by the X-ray diffraction[56] can be shown to be dynamic. The excited motion is the conformational change in an asymmetric potential with a difference energy of ca. 3 kJ mol^{-1}.

The above asymmetric potential model is also consistent with the ^{1}H M_2 observed in **8**, as shown in Fig. 32. The gradual M_2 decrease observed in a wide-temperature range is unusual and cannot be explained by a simple Arrhenius-type activation process. When the double-well potential is introduced, the $M_2{}^{\mathrm{mot}}$ is given by[63]

$$M_2{}^{\mathrm{mot}} = \sum M_2{}^{\mathrm{rig}_{jk}} \frac{1}{(1+a)^2}\left[a^2 + a(3\cos^2 2\theta_{jk} - 1) + 1\right]. \qquad (18)$$

Substituting foregoing values of parameters, an M_2 temperature dependence was obtained as shown in Fig. 32. The agreement with the experiment was not enough, but the qualitative trend of the gradual temperature dependence could be reproduced.

In this section, the monoclinic phase of **2** with $C2/m$ was shown to be a metastable phase which transforms into a stable orthorhombic phase (*Ibam*) at 381 K. The puckering motion between δ and λ conformations in Pt(en)$_2$ moieties was detected in **2** and **8** in the monoclinic phase containing disordered conformations in chelate rings. The two-site jumps under two asymmetric potential wells with the energy differences of 3–5 kJ mol^{-1} were shown in Pt(en)$_2$ chelate rings, indicating that the disordered structure is dynamic between the nonequivalent lattice sites.

7.2 Ligand Reorientations in a Highly-Asymmetric Double-Well Potential Formed in [Pt(en)$_2$][PtX$_2$(en)$_2$](ClO$_4$)$_4$ (X: Cl, Br). In Sec. 7.1, the presence of the order–disorder type phase transition was shown in **8** and a metastable state in **2**, in which the chelate rings in Pt(en)$_2$ moieties take a dynamically disordered structure above the phase transition points. Analogous phase transitions accompanied by the conformation change of chelate rings have been shown in stable phases of [Pt(en)$_2$][PtX$_2$(en)$_2$](ClO$_4$)$_4$ (X: Cl (**9**), Br (**2**)) at 293.2 and 298.7 K,[15,53] respectively. A marked difference from the previous system is that the en conformations in both phases above and below the transition are ordered in the stable phase, but the conformations are transformed from δ–λ or λ–δ in the low-temperature monoclinic phase ($P2_1/m$) to λ–λ or δ–δ in the high-temperature orthorhombic phase (*Ibam*).[15,53] In Secs. 2 and 3, it was shown that ^{1}H NMR T_1 and the diffusion rate (D^*) of neutral solitons decrease upon heating to T_{tr}. This unusual behavior was attributed to the thermal motions of the lattice caused by the phase transition. In this section, dynamics of 1-D chains in the neighborhood of T_{tr} is discussed based on ^{1}H and ^{2}H NMR data.[65]

^{2}H NMR spectra observed in [Pt(NH$_2$(CD$_2$)$_2$NH$_2$)$_2$]-[PtCl$_2$(NH$_2$(CD$_2$)$_2$NH$_2$)$_2$](ClO$_4$)$_4$ (**9-CD**) and [Pt(ND$_2$-(CH$_2$)$_2$ND$_2$)$_2$][PtCl$_2$(ND$_2$(CH$_2$)$_2$ND$_2$)$_2$](ClO$_4$)$_4$ (**9-ND**) are given in Fig. 33. All spectra observed could be explained well by the model of almost rigid C–D and N–D groups in both phases and no marked sign of en motions were observed. In temperature dependence curves of ^{2}H $T_{1\mathrm{D}}$ shown in Fig. 34, however, both analogs gave a broad $T_{1\mathrm{D}}$ minimum at ca. 320 K just above T_{tr} implying the onset of some motion. Since this behavior is quite analogous to those in **8-CD** and **8-ND** given in Fig. 31, chelate-ring motions similar to those in **8** and metastable **2** can be expected. This expectation is, however, in conflict with no C–D and N–D motions expected from ^{2}H spectra and also the ordered structure determined by the X-ray diffraction.[15] A marked difference was that **9-CD** and **9-ND** gave $T_{1\mathrm{D}}$ minima about ten times longer than those in **8** implying much smaller fluctuations of efg caused in **9-CD** and **9-ND**. Since the conformational changes observed in **8** and metastable **2** take place between asymmetric potential wells, a more highly asymmetric potential model is favorable for solving this problem in **9**. Since en conformations in Pt(en)$_2$ are changed from the δ–λ or λ–δ form in the low-temperature phase into the λ–λ or δ–δ form in the high-temperature phase, the δ and λ conformations can be assumed to have different energies in crystals. In case this energy difference (ΔE) is much higher than the thermal energy, so the population in the high-energy conformation should become much lower than that in the stable form. This motional model in potential wells with a high asymmetry can give a shallow $T_{1\mathrm{D}}$ minimum, and at the same time, quite small changes in ^{2}H spectra and also in X-ray diffraction patterns.

If one assumes that $T_{1\mathrm{D}}$ is dominated by the fluctuation of efg caused by the puckering motion between two en conformations in a nonequivalent double-minimum potential shown in Fig. 29, $T_{1\mathrm{D}}$ can be expressed as Eq. 17. Using the relations given by Eqs. 14 and 15 for the asymmetric potential, Eq. 17 was fitted to observed data in Fig. 34. The best fitted calculated $T_{1\mathrm{D}}$ values and determined parameters are shown in Fig. 34 and Table 5, respectively, where 2θ values were obtained from the $T_{1\mathrm{D}}$ minimum values using Eq. 17 to be 68° and 28.5° for jumps of C–D and N–D directions. It is noted that the determined ΔE values are much higher than 2–5 kJ mol^{-1} in **8** and metastable **2** given

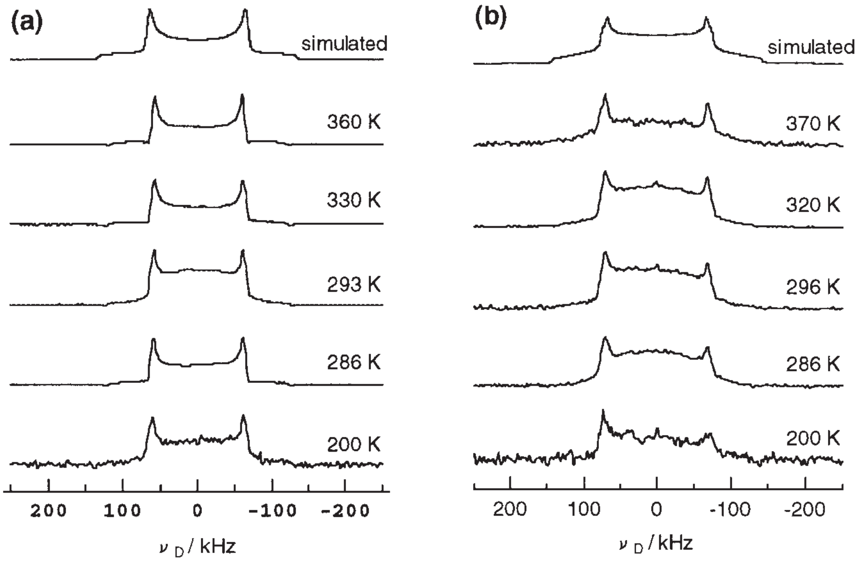

Fig. 33. ^{2}H NMR spectra observed in (a) $[Pt(NH_2(CD_2)_2NH_2)_2][PtCl_2(NH_2(CD_2)_2NH_2)_2](ClO_4)_4$ (**9-CD**) and (b) $[Pt(ND_2(CH_2)_2ND_2)_2][PtCl_2(ND_2(CH_2)_2ND_2)_2](ClO_4)_4$ (**9-ND**). Top spectra in (a) and (b) are simulated for the highest-temperature spectra observed.

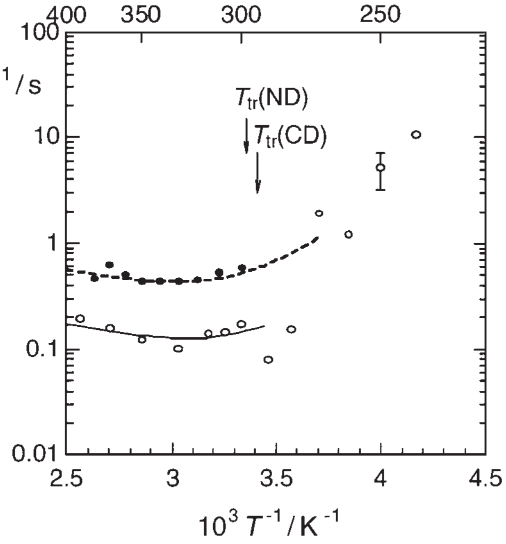

Fig. 34. Temperature dependences of ^{2}H NMR spin-lattice relaxation times (T_{1D}) in $[Pt(NH_2(CD_2)_2NH_2)_2][PtCl_2(NH_2(CD_2)_2NH_2)_2](ClO_4)_4$ (**9-CD**) (○) and $[Pt(ND_2(CH_2)_2ND_2)_2][PtCl_2(ND_2(CH_2)_2ND_2)_2](ClO_4)_4$ (**9-ND**) (●). Broken and solid lines are the best-fitted theoretical values. T_{tr}(CD) and T_{tr}(ND) are phase transition temperatures in **9-CD** and **9-ND**, respectively.

in Table 4. This difference is attributable to the loose crystal packing in **8**, favoring the easily puckering motion. In fact, X-ray and neutron diffraction studies on **8** showed that the steric hindrance for the conformation changes of en ligands is smaller than that in **9**.[15,55,56]

From the above results, the following motional model can be derived: Most en ligands take the stable conformations in both the low- and the high-temperature phase. The puckering motion of the ligand occurs in a highly asymmetric double-well potential, and hence, the lifetime in the unstable conformation is quite short, and its population is low, giving only a slight change in ^{2}H spectra and X-ray diffraction patterns. In fact, ^{2}H spectra calculated under these motional conditions shown in Fig. 33 agree well with the observed spectra.

^{1}H T_{1H} values observed in the neighborhood of T_{tr} for **9** and **2** are shown in Fig. 35. The T_{1H} minimum observed in the two complexes assignable to the above puckering motion of chelate rings was analyzed by use of the asymmetric potential model. The fitting of Eqs. 13–15 was applied to data obtained in the high-temperature phase. The best-fitted T_1 and obtained parameters are shown in Fig. 35 and Table 5, respectively. The fact that ΔE and E_a values evaluated from T_{1H} contributed from magnetic dipolar interactions agreed well with those from T_{1D} determined by electric quadrupolar interactions indicates the adequacy of the present analysis. ΔM_2 values derived from this fitting shown in Table 5 were confirmed by calculating Eq. 16 using crystal data of **2**.[15] The calculated value of 0.120 mT^2 was in good agreement with those derived from T_{1H} given in Table 5.

In the low-temperature phase of **9**, observed temperature dependences of T_{1H} shown in Fig. 35 were fitted by Eqs. 13–15. It is noted that the observed Larmor frequency dependence is inconsistent with the BPP theory requiring the ω^2 dependence.[60] This was explained by introducing jumping between two different energy sites. The fitted T_{1H} curve and obtained parameters are shown in Fig. 35 and Table 5, respectively. From these results, the occurrence of the puckering motion was also shown in the low-temperature phase. The presence of this motion in the low-temperature phase can explain the decreases observed in ^{1}H T_1 and D^* of neutral solitons upon heating as described in Secs. 2 and 3.

From the analysis of ^{2}H NMR spectra and T_{1D} as well as ^{1}H T_{1H} observed around T_{tr} in the stable phases of **2** and **9**, the puckering motion in $Pt(en)_2$ moieties was shown to occur in a highly asymmetric double-well potential with high energy differences of 10–13 kJ mol^{-1} in both high- and low-tempera-

Table 5. Activation Energies (E_a), Potential Energy Differences (ΔE), Reductions of ^{1}H NMR Second Moments (ΔM_2), Motional Constants (C), and Correlation Times at the Infinite Temperature (τ_0) of the Puckering Motion of Pt(en) Chelate Rings in Asymmetric Potential Wells in $[Pt(en)_2][PtX_2(en)_2](ClO_4)_4$ Determined from ^{2}H and ^{1}H NMR Relaxation Times Obtained in the High-Temperature Phase

Compound	E_a/kJ mol^{-1}	ΔE/kJ mol^{-1}	ΔM_2/mT^2	$C/10^9$ s^{-2}	$\tau_0/10^{-13}$ s
$[Pt(NH_2(CD_2)_2NH_2)_2][PtCl_2(NH_2(CD_2)_2NH_2)_2](ClO_4)_4$ (**9-CD**)	32.4 ± 1.0	12.8 ± 0.5	—	62.0 ± 5	6.6 ± 2.0
$[Pt(ND_2(CH_2)_2ND_2)_2][PtCl_2(ND_2(CH_2)_2ND_2)_2](ClO_4)_4$ (**9-ND**)	32.7 ± 0.5	13.0 ± 0.5	—	18.3 ± 5	7.0 ± 1.0
$[Pt(NH_2(CH_2)_2NH_2)_2][PtCl_2(NH_2(CH_2)_2NH_2)_2](ClO_4)_4$ (**9**)	31.7 ± 1.0	13.0 ± 1.0	0.13 ± 0.04	6.1 ± 0.5	6.6 ± 1.0
$[Pt(NH_2(CH_2)_2NH_2)_2][PtBr_2(NH_2(CH_2)_2NH_2)_2](ClO_4)_4$ (**2**)	31.0 ± 1.0	13.0 ± 1.0	0.13 ± 0.04	6.1 ± 0.5	6.6 ± 1.0
$[Pt(NH_2(CH_2)_2NH_2)_2][PtCl_2(NH_2(CH_2)_2NH_2)_2](ClO_4)_4$ (**9**)[a]	34.1 ± 1.0	10.2 ± 1.0	0.12 ± 0.04	5.6 ± 0.5	1.4 ± 4.0

a) Low-temperature phase.

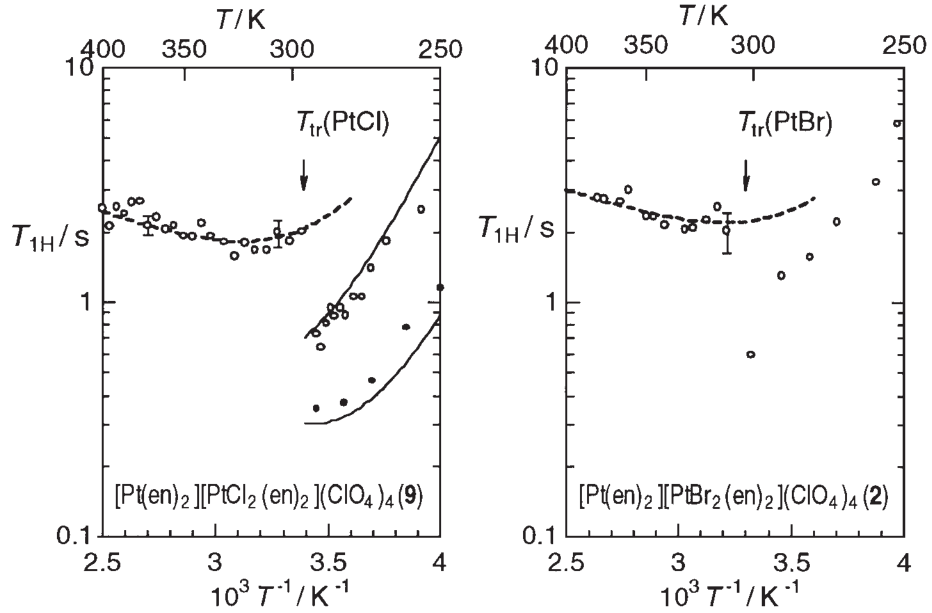

Fig. 35. ^{1}H NMR spin-lattice relaxation times (T_{1H}) observed in $[Pt(en)_2][PtCl_2(en)_2](ClO_4)_4$ (**9**) at Larmor frequency of 54.3 (○) and 21.3 (●) MHz and $[Pt(en)_2][PtBr_2(en)_2](ClO_4)_4$ (**2**) at 54.3 MHz. Broken and solid lines are the best-fitted theoretical values. T_{tr}(PtCl) and T_{tr}(PtBr) are phase transition temperatures in **9** and **2**, respectively.

ture sides of T_{tr}.

8. Valence Structures of 1-D Halogen-Bridged MMX-Type Complexes, $A_4[Pt_2X(pop)_4]\cdot nH_2O$ Studied by ^{31}P Solid NMR

Recently developed new-types of halogen-bridged 1-D complexes containing binuclear metal units called *MMX chain* have been shown[66] to be able to form complex valence structures expressed as:

(**A**) $-M^{2+}-M^{2+}-X-M^{3+}-M^{3+}-X-$ (CDW State)

(**B**) $-M^{2+}-M^{3+}-X-M^{2+}-M^{3+}-X-$ (Charge Polarization State)

(**C**) $-M^{2+}-M^{3+}-X-M^{3+}-M^{2+}-X-$ (Alternate Charge-Polarization State)

(**D**) $-M^{2.5+}-M^{2.5+}-X-M^{2.5+}-M^{2.5+}-X-$ (Averaged-Valence State)

In structure **A**, since all electron spins in d-orbitals in M are paired, a diamagnetic 1-D chain is formed, while **B** and **D** can contain unpaired spins giving paramagnetic properties. In case **C** takes a spin-Peierls state, two unpaired spins in neighboring M^{3+} sites are cancelled, giving vanishing paramagnetism.

$A_4[Pt_2X(pop)_4]\cdot nH_2O$, where A, pop, and X are alkaline or alkaline earth metals, diphosphite ion ($P_2O_5H_2{}^{2-}$), and halogens (Cl, Br, I), respectively, have been reported to form MMX-type chain complexes.[67] As an example of MMX-type chain complexes, the structure of $(NH_4)_4[Pt_2Cl(pop)_4]$ is shown in Fig. 36. From the presence of metal–metal bonds in 1-D chains, complicated magnetic and electric properties compared with those in MX chains can be expected in the MMX complexes. To determine the valence structures in MMX chains, the solid NMR measurement of ^{31}P in pop ligands is quite suitable, because the nonequivalency of metal sites and the presence of unpaired spins can easily be detected by measuring MAS NMR spectra of ^{31}P ($I = 1/2$) and its relaxation behavior, respectively.

8.1 Spin Structures in $(NH_4)_4[Pt_2X(pop)_4]$ (X: Cl, Br, I). ^{31}P MAS NMR spectra observed in polymer complexes $(NH_4)_4[Pt_2X(pop)_4]$ (X: Cl, Br, I) at room temperature are shown in Fig. 37.[68] For comparison, spectra for monomer complexes $[Pt_2(pop)_4]^{4-}$ and $[Pt_2X_2(pop)_4]^{4-}$ consisting of the binuclear Pt^{2+} and Pd^{3+} unit, respectively, are shown in Figs. 38 and 39 in the same order. Observed chemical shifts δ and spin–

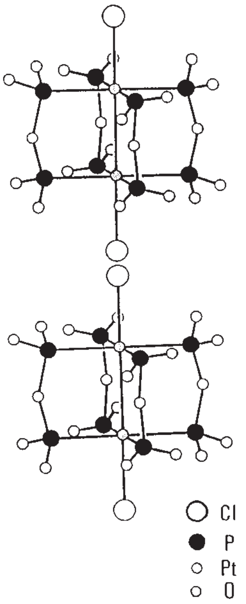

Fig. 36. A structure of a 1-D MMX-type polymer complex, $(NH_4)_4[Pt_2Cl(P_2O_5H_2)_4]$. Atomic arrangements only in anions are shown. Positions of the bridged chlorine atoms disordered over two sites in the chain are observed by the X-ray diffraction (Ref. 68).

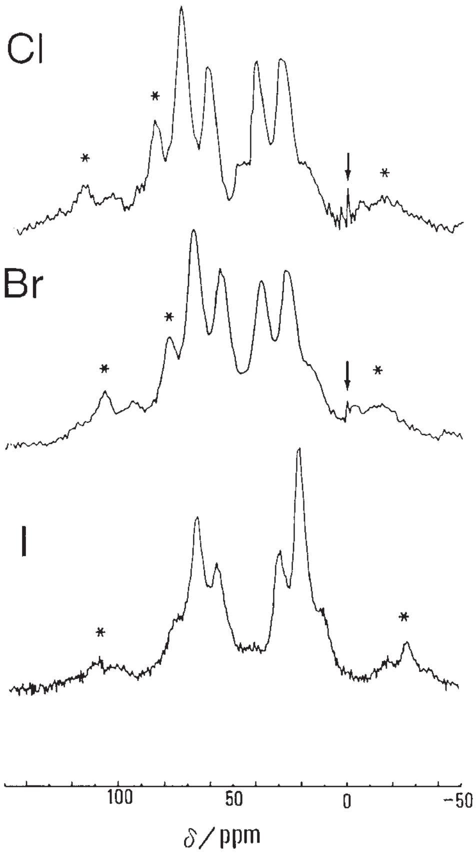

Fig. 37. ^{31}P MAS NMR spectra of MMX-type polymer complexes, $(NH_4)_4[Pt_2X(P_2O_5H_2)_4]$ (X: Cl, Br, I). Peaks with asterisks are spinning sidebands. Arrows show the signal of PO_4^{3-} impurity which was used as the internal standard.

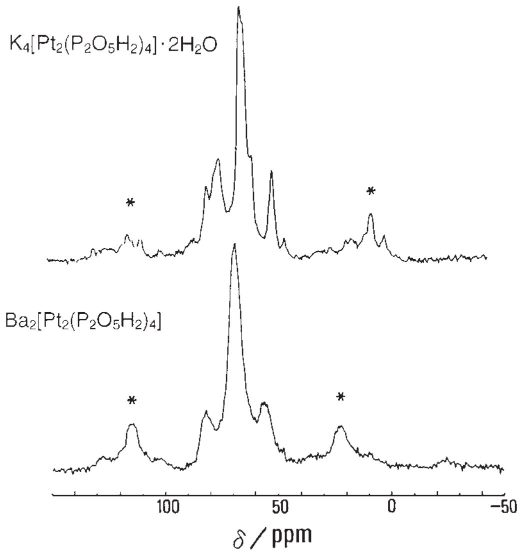

Fig. 38. ^{31}P MAS NMR spectra of monomer Pt^{2+} complexes: $K_4[Pt_2(P_2O_5H_2)_4]\cdot 2H_2O$ and $Ba_2[Pt_2(P_2O_5H_2)_4]$. Satellite lines on both sides of the peak are splitting by the coupling between ^{31}P and ^{125}Pt. Peaks with asterisks are spinning sidebands.

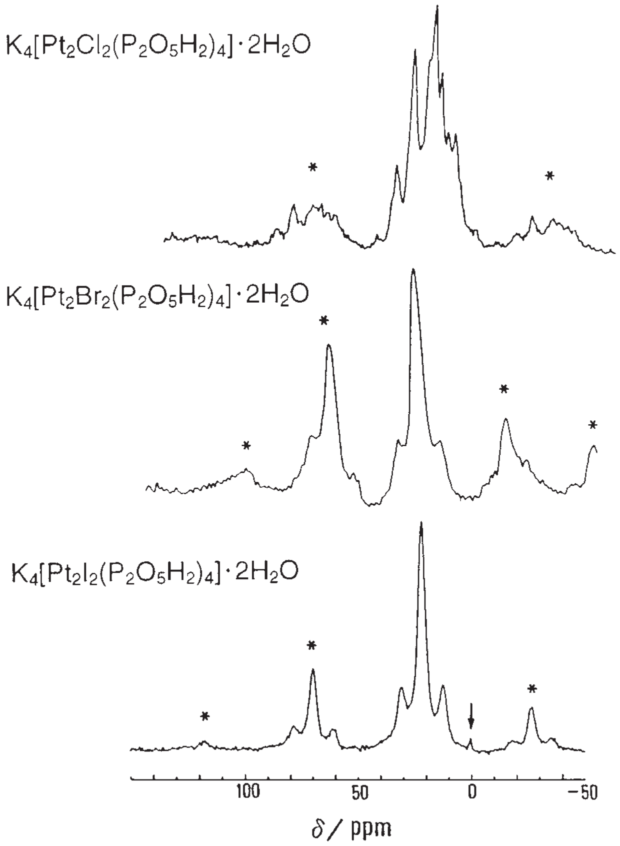

Fig. 39. ^{31}P MAS NMR spectra of monomer Pt^{3+} complexes: $K_4[Pt_2Cl_2(P_2O_5H_2)_4]\cdot 2H_2O$, $K_4[Pt_2Br_2(P_2O_5H_2)_4]\cdot 2H_2O$ and $K_4[Pt_2I_2(P_2O_5H_2)_4]\cdot 2H_2O$. Satellite lines on both sides of the peak are splitting by the coupling between ^{31}P and ^{125}Pt. Peaks with asterisks are spinning sidebands.

Table 6. ^{31}P Chemical Shifts (δ) and Coupling Constants ($J_{\text{Pt–P}}$) in –X–Pt–Pt–X–Pt–Pt–X– Type MMX Complexes Together with Binuclear Pt^{2+} and Pt^{3+} Monomer Complexes Observed by MAS NMR at Room Temperature

	Compound	δ/ppm a)		$J_{\text{Pt–P}}$/kHz
Polymer	$(NH_4)_4[Pt_2Cl(P_2O_5H_2)_4]$	27 ± 4.6	59 ± 2.2	
		38 ± 1.8	70 ± 3.0	
	$(NH_4)_4[Pt_2Br(P_2O_5H_2)_4]$	24 ± 3.5	53 ± 1.5	
		36 ± 1.5	65 ± 2.0	
	$(NH_4)_4[Pt_2I(P_2O_5H_2)_4]$	19 ± 2.6		2.3 ± 0.5
			65 ± 1.7	2.5 ± 0.5
Monomer (Pt^{2+})	$K_4[Pt_2(P_2O_5H_2)_4]\cdot 2H_2O$		65 ± 2.0	3.4 ± 0.1
	$Ba_2[Pt_2(P_2O_5H_2)_4]$		66 ± 2.0	3.2 ± 0.5
(Pt^{3+})	$K_4[Pt_2Cl_2(P_2O_5H_2)_4]\cdot 2H_2O$	12 ± 0.6		
		15 ± 0.9		
		17 ± 0.8		
		24 ± 1.0		
	$K_4[Pt_2Br_2(P_2O_5H_2)_4]\cdot 2H_2O$	27 ± 3.0		2.2 ± 0.3
	$K_4[Pt_2I_2(P_2O_5H_2)_4]\cdot 2H_2O$	21 ± 2.5		2.2 ± 0.5

a) Chemical shifts were measured from an 85% aqueous H_3PO_4.

spin coupling constants J are given in Table 6. Monomer complexes, $K_4[Pt_2(pop)_4]\cdot 2H_2O$ and $Ba_2[Pt_2(pop)_4]$ of Pt^{2+}, and $K_4[Pt_2X_2(pop)_4]\cdot 2H_2O$ (X: Br, I) of Pt^{3+} gave a single ^{31}P line with a pair of satellites due to the coupling between ^{31}P and ^{195}Pt ($I = 1/2$, the natural abundance of 33.8%). This indicates that all P atoms in crystals are equivalent, in good agreement with the reported crystal structures.[69] On the other hand, $K_4[Pt_2Cl_2(pop)_4]\cdot 2H_2O$ gave four overlapped independent lines consistent with the crystal structure data[70] requiring four nonequivalent P sites. A clear difference in δ between Pt^{2+} and Pt^{3+} is explainable by the difference in paramagnetic shift δ_P proportional to the reciprocal of electronic excitation energies (ΔE) from the ground state.[71] Spectroscopic studies in solutions of these two kinds of complexes[67,72] showed that the Pt^{3+} complex has a higher ΔE than in that in Pt^{2+}, consistent with the present ^{31}P solid NMR results. Since J values have been shown[73] to decrease with the increase in the coordination number of coupled metals, the fact that four-coordinated Pt^{2+} complexes gave a J value larger than those in six-coordinated Pt^{3+} complexes agrees well with this general rule.

As shown in Fig. 37, the polymer iodo-complex gave a pair of lines, while polymer chloro- and bromo-complexes afforded two pairs of peaks. Shift values of the two lines in the former-complex and averaged shift values in respective pairs in latter complexes were close to those in Pt^{2+} and Pt^{3+} monomer complexes as shown in Table 6. Since the presence of two crystallographically nonequivalent P sites in each $Pt_2(pop)_4$ unit was reported in Cl and Br complexes,[70] splittings of ca. 10 ppm observed in these complexes were attributed to the two kinds of P sites placed in different crystal fields. From the obtained data that chemical shift values observed in all polymer complexes shown in Table 6 were close to those in Pt^{2+} and Pt^{3+} monomer complexes, the presence of two kinds of P atoms differently coordinated to Pt sites could be concluded. This result indicates that polymer complexes $(NH_4)_4[PtX(pop)_4]$ consist of Pt^{2+} and Pt^{3+} sites with almost the same concentration. This result suggests a low possibility of the averaged-valence structure (**D**).

To determine the most probable structure, ^{31}P NMR relaxation time (T_1) measurements were performed at room temperature. The monomer complexes of Pt^{2+} and Pt^{3+} having no unpaired spins gave long ^{31}P NMR T_1 of ca. 40 and 100 s for $K_4[Pt_2(pop)_4]$ and $K_4[Pt_2I_2(pop)_4]\cdot 2H_2O$, respectively. These values are quite normal for diamagnetic crystals without marked molecular motions. The polymer complex $(NH_4)_4[Pt_2I(pop)_4]$ showed superimposed T_1 of two components, 0.5 ± 0.2 and 100 ± 20 s. The other chloro- and bromo-complexes also gave analogous results. Since the long T_1 component was major, most complex ions are diamagnetic supporting the CDW $-M^{2+}-M^{2+}-X-M^{3+}-M^{3+}-X-$ chains given by (**A**). The possibility of (**C**) could not be accepted from crystal structures.[74,75] The short T_1 component observed in the iodo-complex seems to be attributed to the mixing of the structure (**D**), which was suggested to be formed from Raman and XP spectrum measurements.[76] The present conclusion of the spin structure of pop complexes derived from ^{31}P NMR agree well with the result of X-ray diffraction studies.[75]

8.2 Spin Structures in $R_4[Pt_2I(pop)_4]$ (R: Li, Na, K, Rb, Cs). It has recently been suggested from Raman and XP spectrum measurements[76] that the spin structure in polymer complexes of $[Pt_2I(pop)_4]^{4-}$ is markedly affected by the crystal packing. To reveal the problem, ^{31}P solid NMR spectra and T_1 were measured for this complex with various counter cations for obtaining effects from the packing of complex ions in crystals. ^{31}P MAS NMR spectra observed in $R_4[Pt_2I(P_2O_5H_2)_4]\cdot nH_2O$ (R: Cs ($n = 0$), Rb ($n = 2$), K ($n = 2$), Na ($n = 2$), Li ($n = 4$)) at room temperature are shown in Fig. 40.[77] Clearly separated and almost overlapped two doublet peaks were observed in Cs and Rb salts, respectively. Chemical shift values at the centers of the respective doublets were 60 and 26 ppm for the Cs salt, and 58 and 26 ppm for the Rb salt. These values could be explained well by pop ligands coordinated to Pt^{2+} and Pt^{3+} from the analysis given in Sec. 8.1.[68] These results imply that Cs and Rb salts form 1-D chains of the CDW state (**A**) analogous to those in $(NH_4)_4[Pt_2X(pop)_4]$ given above. Observed doublets are attributable to splittings due to the crystal field.

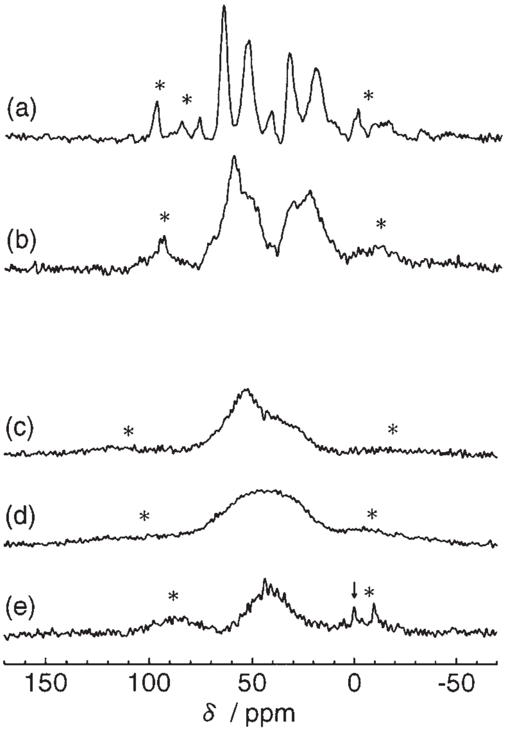

Fig. 40. ^{31}P MAS NMR spectra in (a) $Cs_4[Pt_2I(P_2O_5H_2)_4]$, (b) $Rb_4[Pt_2I(P_2O_5H_2)_4]\cdot 2H_2O$, (c) $K_4[Pt_2I(P_2O_5H_2)_4]\cdot 2H_2O$, (d) $Na_4[Pt_2I(P_2O_5H_2)_4]\cdot 2H_2O$ and (e) $Li_4[Pt_2I(P_2O_5H_2)_4]\cdot 4H_2O$. Peaks with asterisks are spinning sidebands. The arrow shows the signal of PO_4^{3-} impurity used as the internal standard.

On the other hand, Li and Na salts afforded only a broad single line at ca. 42 and 45 ppm, respectively, corresponding to nearly the mean shift value between those in Pt^{2+} and Pt^{3+} states. This suggests that the averaged-valence structure (**D**) is acceptable for Li and Na salts. Since the time scale in the NMR measurement is slow, the possibility of the observation of a dynamically averaged structure cannot be excluded when electron spins rapidly jump between Pt^{2+} and Pt^{3+} sites.

The ^{31}P T_1 measurement at room temperature gave ca. 0.7 s (Cs), 0.1–0.9 s (Rb), 0.1 s (K), 70 ms (Na), and 70 ms (Li). This order agrees with that in the spectrum line-width seen in Fig. 40. Since the short T_1 values in Li and Na salts imply the marked contribution from the fluctuation of paramagnetic spins, this result is in good agreement with the above spectrum analysis, supporting the model (**D**). Rather long T_1 in Cs and Rb salts is assignable to the diamagnetic structure model, but their T_1 values are much shorter than 10–100 s in monomer complexes and ammonium salts discussed in the previous section. This difference suggests the presence of dynamic mixing of a small amount of paramagnetic structures with the main CDW spin structure. This effect can more markedly be seen in the K salt, which showed intermediate values in all of the spectrum line-width, its splitting and T_1 explainable by the mixing of structures. The continuous dependencies of the line-width and T_1 upon the cationic size and the number of crystalline water are explainable by considering that intra- and/or inter-chain spin jumps are affected by hydrogen bonds and chain packings in crystals.

9. Concluding Remarks

Electron-spin structures and dynamics in halogen-bridged 1-D complexes were effectively studied by the measurement of the solid NMR line-shape and the spin-lattice relaxation. By noticing that an electron spin having a magnetic moment much larger than that of a proton can give strong effects on NMR spectra and relaxations, NMR was shown to be a quite sensitive probe to monitor structures and dynamics of electron spins formed along the 1-D chains. Even a quite low concentration of paramagnetic spins of the order of 10^{-3} to 10^{-4} in molar ratio was revealed to cause a marked change in the NMR relaxation, which enabled us to follow a small amount of neutral solitons and polarons diffusing along the chains in CDW complexes. Dynamical parameters for the migration of neutral solitons were derived from relaxation data. A diffusion rate comparable to that in *trans*-polyacetylene was obtained in CDW Pd and Pt MX complexes.

Observations of high-resolution solid-NMR spectra of ^{13}C and ^{31}P were shown to afford detailed information of the microscopic 1-D structure and spin fluctuations on metal sites in MX and MMX-type chain complexes.

The high sensitivity of NMR for the detection of paramagnetic spins may sometimes give quite broad spectra or too short T_1 unaccessible by conventional NMR techniques, as observed in isolated paramagnetic molecules in solid. In the present averaged-valence complexes $[NiX(chxn)_2]X_2$, despite a high concentration of paramagnetic Ni sites, sharp spectra and moderate T_1 values convenient for the measurement and analysis were obtained. This is because a quite strong antiferromagnetic coupling between neighboring spins suppresses the fluctuation of magnetic field at NMR nuclei. Dynamic magnetic properties in $S = 1/2$ 1-D Heisenberg systems at low temperature range were obtained from the relaxation and spectrum analysis. The highest value of exchange interactions (J) in 1-D antiferromagnetic systems so far reported was obtained in $[NiBr(chxn)_2]Br_2$.

Thermal motions of 1-D chains associated with structural phase transitions were successfully studied by NMR spectrum and relaxation analyses. Puckering motions of $Pt(en)_2$ moieties, accompanied by the ethylenediamine (en) conformation changes, which are undetectable by the X-ray diffraction or the NMR spectrum analysis, were observed by the relaxation measurement and proved to occur in a highly asymmetric double-well potential.

These works were performed in groups of magnetic resonances in Nagoya University (1987–1990), Institute of Molecular Science (1988–90) and University of Tsukuba (1990–2003) in collaboration with many co-workers including students. The author is really grateful for their cooperation. He appreciates discussions with Prof. Noriyoshi Kimura in Wakayama University, Prof. Masahiro Yamashita and Dr. Sinya Takaishi in Tokyo Metropolitan University, Prof. Hiroshi Kitagawa in Kyushu University, Prof. Koshiro Toriumi in Himeji Institute of Technology, Dr. Shin'ichi Ishimaru in University of Tsukuba, Prof. Tetsuo Asaji in Nihon University, the late Prof. Daiyu Nakamura in Nagoya University, the late Prof. Alarich Weiss in Darmstadt Technische Hochschule, Dr. Hiroshi Ohki in Hiroshima University, Dr. Ashutosh Ghosh in University of

Calcutta, Dr. L. S. Prabhumirashi in University of Pune, and Mr. Masaki Iida, Mr. Hidenori Suzuki, Mr. Yukitaka Nakano, Mr. Toru Hachisuka, Mr. Masataka Kano, and Mr. Akio Ozawa in Nagoya University and University of Tsukuba.

References

1 J. S. Miller and A. J. Epstein, *J. Prog. Inorg. Chem.*, **20**, 1 (1976); H. J. Keller, "Extended Linear Chain Compounds," ed by J. S. Miller, Plenum Press, New York (1982), Vol. 1, p. 357; R. J. H. Clark, "Mixed-Valence Compounds," ed by D. B. Brown, Reidel, Dordrecht (1982), p. 271.

2 N. Matsumoto, M. Yamashita, and S. Kida, *Bull. Chem. Soc. Jpn.*, **51**, 2334 (1978); M. Yamashita, Y. Nonaka, S. Kida, Y. Hamaue, and R. Aoki, *Inorg. Chim. Acta*, **52**, 43 (1981); M. Yamashita, H. Ito, K. Toriumi, and T. Ito, *Inorg. Chem.*, **22**, 1566 (1983); M. Yamashita and I. Murase, *Inorg. Chim. Acta*, **97**, L43 (1985).

3 D. Hall and P. P. Williams, *Acta Crystallogr.*, **11**, 624 (1958); K. P. Larsen and H. Toftlund, *Acta Chem. Scand.*, **A31**, 182 (1977); M. Yamashita, N. Matsumoto, and S. Kida, *Inorg. Chim. Acta*, **31**, 381 (1978); A. L. Beauchamp, D. Layek, and T. Theophanides, *Acta Crystallogr.*, **B38**, 1158 (1982).

4 H. Endres, H. J. Keller, R. Martin, U. Traeger, and N. Novotny, *Acta Crystallogr.*, **B36**, 35 (1980).

5 W. P. Su, J. R. Schrieffer, and A. J. Heeger, *Phys. Rev. Lett.*, **42**, 1698 (1979).

6 K. Nasu and Y. Toyozawa, *J. Phys. Soc. Jpn.*, **51**, 2098 (1982); **51**, 3111 (1982).

7 K. Toriumi, Y. Wada, T. Mitani, S. Bandow, M. Yamashita, and Y. Fujii, *J. Am. Chem. Soc.*, **111**, 2341 (1989). Figure 1 is reprinted with permission from American Chemical Society (Copyright 1989).

8 H. Okamoto, K. Toriumi, T. Mitani, and M. Yamashita, *Phys. Rev.*, **B42**, 10381 (1990). Figure 2 is reprinted with permission from the American Physical Society (Copyright 1990).

9 W. P. Su, J. R. Schrieffer, and A. J. Heeger, *Phys. Rev.*, **B22**, 2099 (1980).

10 A. Kawamori, R. Aoki, and M. Yamashita, *J. Phys. C*, **18**, 5487 (1985).

11 N. Kimura, S. Ishimaru, R. Ikeda, and M. Yamashita, *J. Chem. Soc., Faraday Trans.*, **94**, 3659 (1998).

12 F. Devreux, J.-P. Boucher, and M. Nechtschein, *J. Phys. (Paris)*, **35**, 271 (1974).

13 F. Devreux, *Phys. Rev.*, **B25**, 6609 (1982).

14 M. Yamashita, K. Toriumi, and T. Ito, *Acta Crystallogr.*, **C41**, 876 (1985).

15 K. Toriumi, M. Yamashita, S. Kurita, I. Murase, and T. Ito, *Acta Crystallogr.*, **B49**, 497 (1993).

16 Y. Hamaue, R. Aoki, M. Yamashita, and S. Kida, *Inorg. Chim. Acta*, **54**, L13 (1981).

17 M. Nechtschein, F. Devreux, R. L. Greene, T. C. Clarke, and G. B. Street, *Phys. Rev. Lett.*, **44**, 356 (1980).

18 R. Ikeda, M. Iida, T. Asaji, A. Ghosh, and M. Yamashita, *Chem. Phys. Lett.*, **210**, 78 (1993).

19 A. Mishima and K. Nasu, *Phys. Rev.*, **B39**, 5758 (1989).

20 A. Mishima and K. Nasu, *Phys. Rev.*, **B39**, 5763 (1989).

21 M. Suzuki and K. Nasu, *Phys. Rev.*, **B45**, 1605 (1992).

22 N. Matsumoto, M. Yamashita, and S. Kida, *Bull. Chem. Soc. Jpn.*, **51**, 2334 (1978).

23 K. Toriumi, M. Yamashita, and I. Murase, *Chem. Lett.*, **1986**, 1753.

24 N. Kimura, H. Suzuki, T. Kawashima, T. Manabe, M. Yamashita, and R. Ikeda, *Synth. Met.*, **103**, 2604 (1999).

25 H. Okamoto, Y. Kaga, Y. Shimada, Y. Oka, Y. Iwase, T. Mitani, and M. Yamashita, *Phys. Rev. Lett.*, **80**, 861 (1998).

26 H. Okamoto, T. Mitani, K. Toriumi, and M. Yamashita, *Mater. Sci. Eng.*, **B13**, L9 (1992).

27 K. Toriumi, unpublished data.

28 Y. Wada, T. Mitani, M. Yamashita, and T. Koda, *J. Phys. Soc. Jpn.*, **54**, 3143 (1985).

29 M. Nechtschein, F. Devreux, F. Genoud, M. Guglielmi, and K. Holczer, *Phys. Rev.*, **B27**, 61 (1983).

30 H. Okamoto, unpublished data.

31 T. Manabe, M. Yamashita, T. Kawashima, H. Okamoto, H. Kitagawa, T. Mitani, K. Toriumi, H. Miyamae, K. Inoue, and K. Yakusi, *Proc. SPIE*, **3145**, 106 (1998).

32 H. Toftlund, P. W. Jensen, and C. S. Jacobsen, *Chem. Phys. Lett.*, **142**, 286 (1987).

33 A. Ozawa, N. Kimura, H. Kitagawa, and R. Ikeda, *Synth. Met.*, **135–136**, 419 (2002).

34 K. Toriumi, H. Okamoto, T. Mitani, S. Bandow, M. Yamashita, Y. Wada, Y. Fujii, R. J. H. Clark, D. J. Michael, A. J. Edward, D. Watkins, M. Kurmoo, and P. Day, *Mol. Cryst. Liq. Cryst.*, **181**, 333 (1990).

35 R. Ikeda, T. Tamura, and M. Yamashita, *Chem. Phys. Lett.*, **173**, 466 (1990). Figures 1 and 2 are reprinted with permission from Elsevier (Copyright 1990).

36 J. E. Sarneski, H. L. Surprenant, F. K. Molen, and C. N. Reilley, *Anal. Chem.*, **47**, 2116 (1975).

37 D. R. Eaton and W. D. Phillips, "Advances in Magnetic Resonance," ed by J. S. Waugh, Academic Press, New York (1965), Vol. 1, p. 103.

38 R. Ikeda, unpublished data.

39 H. Rager, *Z. Naturforsch.*, **36a**, 637 (1981); J. Czaplicki, N. Weiden, and A. Weiss, *Physica*, **B154**, 93 (1988).

40 J. C. Bonner and M. E. Fisher, *Phys. Rev.*, **135**, A640 (1964).

41 A. W. Sandvik, *Phys. Rev.*, **B52**, R9831 (1995); V. Barzykin, *Phys. Rev.*, **B63**, 140412(R) (2001).

42 S. Sachdev, *Phys. Rev.*, **B50**, 13006 (1994).

43 S. Takaishi, Y. Furukawa, K. Kumagai, and R. Ikeda, *Synth. Met.*, **135–136**, 401 (2003).

44 D. B. Brown, J. W. Hall, H. M. Helis, E. G. Walton, D. J. Hodfson, and W. E. Hatfield, *Inorg. Chem.*, **16**, 118 (1977).

45 K. Marumoto, H. Tanaka, S. Kuroda, T. Manabe, and M. Yamashita, *Phys. Rev.*, **B60**, 7699 (1999).

46 M. Yamashita, T. Manade, K. Inoue, T. Kawashima, H. Okamoto, H. Kitagawa, T. Mitani, K. Toriumi, H. Miyamae, and R. Ikeda, *Inorg. Chem.*, **38**, 1894 (1999).

47 N. Motoyama, H. Eisaki, and S. Uchida, *Phys. Rev. Lett.*, **76**, 3212 (1996).

48 N. Bloembergen, E. Purcell, and R. Pound, *Phys. Rev.*, **73**, 679 (1948).

49 A. Hazell, *Acta Crystallogr.*, **C47**, 962 (1991).

50 M. Yamashita, T. Ishii, H. Matsuzaka, T. Manabe, T. Kawashima, H. Okamoto, H. Kitagawa, T. Mitani, K. Marumoto, and S. Kuroda, *Inorg. Chem.*, **38**, 5124 (1999).

51 K. Marumoto, T. Tanaka, S. Kuroda, T. Manabe, and M. Yamashita, *Phys. Rev.*, **B60**, 7699 (1999).

52 N. Kimura, M. Kano, T. Manabe, M. Yamashita, and R. Ikeda, *Synth. Met.*, **120**, 777 (2001).

53 S. C. Huckett, B. Scott, S. P. Love, R. J. Donohoe, C. J. Burns, E. Garcia, T. Frankcom, and B. I. Swanson, *Inorg. Chem.*,

32, 2137 (1993).

54 K. Toriumi, unpublished data.

55 H. Endres, H. J. Keller, R. Martin, H. N. Gung, and U. Traeger, *Acta Crystallogr.*, **B35**, 1885 (1979).

56 J.-F. Bardeau, A. Bulou, W. T. Klooster, T. F. Koetzle, S. Johnson, B. Scott, B. I. Swanson, and J. Eckert, *Acta Crystallogr.*, **B52**, 854 (1996).

57 N. Kimura, T. Hachisuka, Y. Nakano, and R. Ikeda, *Phys. Chem. Chem. Phys.*, **3**, 1778 (2001).

58 J. Seelig, *Quart. Rev. Biophys.*, **10**, 353 (1977); M. J. Hunt and A. L. MacKay, *J. Magn. Reson.*, **15**, 402 (1974).

59 R. Ikeda, A. Kubo, and C. A. MacDowell, *J. Phys. Chem.*, **93**, 7315 (1989).

60 A. Abragam, "The Principles of Nuclear Magnetism," Oxford University Press, Oxford (1961), Chap. VIII.

61 D. C. Look and I. J. Lowe, *J. Chem. Phys.*, **44**, 3437 (1966).

62 J. H. Van Vleck, *Phys. Rev.*, **74**, 1168 (1948).

63 E. R. Andrew and L. Latanowicz, *J. Magn. Reson.*, **68**, 232 (1986).

64 M. Mizuno, Y. Hamada, T. Kitahara, and M. Suhara, *J. Phys. Chem.*, **103**, 498 (1999).

65 N. Kimura, T. Hachisuka, Y. Nakano, and R. Ikeda, *Z. Naturforsch.*, **57a**, 413 (2002).

66 H. Kitagawa, N. Onodera, T. Sonoyama, M. Yamamoto, T. Fukawa, T. Mitani, M. Seto, and Y. Maeda, *J. Am. Chem. Soc.*, **121**, 10068 (1999).

67 C.-M. Che, L. G. Butler, and H. B. Gray, *J. Am. Chem. Soc.*, **103**, 7796 (1981); C.-M. Che, W. P. Schaefer, H. B. Gray, M. K. Dickson, P. B. Stein, and D. M. Roundhill, *J. Am. Chem. Soc.*, **104**, 4253 (1982).

68 N. Kimura, H. Ohki, R. Ikeda, and M. Yamashita, *Chem. Phys. Lett.*, **220**, 40 (1994). Figure 1 is reprinted with permission from Elsevier (Copyright 1994).

69 R. J. H. Clark, M. Kurmoo, H. M. Dawes, and M. B. Hursthouse, *Inorg. Chem.*, **25**, 409 (1986).

70 C.-M. Che, F. H. Herbstein, W. P. Schaefer, R. E. Marsh, and H. B. Gray, *J. Am. Chem. Soc.*, **105**, 4604 (1983).

71 N. F. Ramsey, *Phys. Rev.*, **78**, 699 (1950).

72 C.-M. Che, L. G. Butler, P. J. Grunthaner, and H. B. Gray, *Inorg. Chem.*, **24**, 4662 (1985).

73 I. J. Coloquhoun and W. J. McFarlane, *J. Chem. Soc., Chem. Commun.*, **1980**, 145.

74 L. G. Butler, M. H. Zietlow, C.-M. Che, W. P. Schaefer, S. Sridhar, P. J. Grunthaner, B. I. Swanson, R. J. H. Clark, and H. B. Gray, *J. Am. Chem. Soc.*, **110**, 1155 (1988).

75 S. Jin, T. Ito, K. Toriumi, and M. Yamashita, *Acta Crystallogr.*, **C45**, 1415 (1989).

76 M. Yamashita, S. Miya, T. Kawashima, T. Manabe, T. Sonoyama, H. Kitagawa, T. Mitani, H. Okamoto, and R. Ikeda, *J. Am. Chem. Soc.*, **121**, 2321 (1999).

77 N. Kimura, S. Ishimaru, T. Kawashima, S. Miya, T. Manabe, M. Yamashita, and R. Ikeda, *Synth. Met.*, **120**, 779 (2001).

Ryuichi Ikeda born in Nagoya 1940. Received B.Sc. in 1963, M.Sc. in 1965, and Ph.D. in 1968 from Nagoya University. He was appointed assistant of Department of Chemistry, Nagoya University in 1968, promoted to associate professor in 1980, and moved to Coordination Chemistry Laboratories, Institute for Molecular Science in 1988. He was promoted to full professor of Department of Chemistry, University of Tsukuba in 1990. His research interests have been dynamic properties of electron spins, protons, ions, and molecules in solid. Applying mainly magnetic resonance techniques, i.e., NMR, NQR, and ESR, he has studied dynamics behavior of molecular ions in new mesophases between solid and liquid such as *ionic plastic-crystals* and *rotator phases* consisting of alkylammonium ions, structures and dynamics of ions and molecules adsorbed in one-dimensional tunnel or two-dimensional layer systems, the dynamics of electron spins and the magnetism in halogen-bridged metal complexes, intermolecular proton transfers in hydrogen-bonded solid, etc.